International Journal of Plasticity 27 (2011) 1203–1223

Contents lists available at ScienceDirect

International Journal of Plasticity

journal homepage: www.elsevier.com/locate/ijplas

Void growth and coalescence in ductile solids with stage III and stage IV strain hardening

L. Lecarme *, C. Tekoğlu, T. Pardoen

Institute of Mechanics, Materials and Civil Engineering, Université catholique de Louvain, Place Sainte Barbe 2, B-1348 Louvain-la-Neuve, Belgium

ARTICLE INFO

Article history:
Received 28 July 2010
Received in final revised form 29 November 2010
Available online 27 January 2011

Keywords:
Ductility
Voids and inclusions
Strengthening mechanisms
Constitutive behaviour
Void coalescence

ABSTRACT

State of the art ductile fracture models often rely on simple power laws to describe the strain hardening of the matrix material. Power laws do not distinguish between the two main stages of hardening observed in polycrystals, referred to as stage III and stage IV hardening, and which emerge from the evolution of the dislocation substructure. The aim of this study is to couple a physics based strain hardening law including these two stages to a micromechanics based ductile damage model. One of the main motivations is that, the stage IV constant hardening rate stage, occurring only at large strain, will be attained in most ductile failure problems if not at the overall level of deformation, at least locally around the growing voids. Furthermore, proper modelling of the stage III involving dislocation storage and recovery terms and the transition to stage IV provides a link with the underlying physical mechanisms of deformation and with the microstructure. First, in order to evaluate the effects of the stage III and stage IV hardening on void growth and coalescence, an extensive parametric study is performed on two-dimensional (2D) axisymmetric finite element (FE) unit cell calculations, using a Kocks–Mecking type hardening law. The cell calculations demonstrate that accounting for the stage IV hardening can have a profound effect on delaying void coalescence and increasing the ductility. The magnitude of the recovery term during stage III has also a significant effect on the void growth rate. Then, the Kocks–Mecking law is incorporated into the Gologanu–Leblond–Devaux (GLD) porous plasticity model supplemented by two different versions of the Thomason void coalescence criterion. The predictions of the damage model are in good agreement with the results of the FE calculations in terms of the stress–strain curves, the evolution of void shape and porosity, as well as the strain value at the onset of void coalescence.

1. Introduction

Micromechanics based studies of void growth in ductile materials date back to the late 1960's, with the pioneering works of McClintock (1968), and Rice and Tracey (1969), respectively focusing on the growth of a cylindrical and of a spherical void in an infinite plastically deforming material with no strain hardening. In the same vein, Gurson (1977a) developed a micromechanics based porous plasticity model, which is the most widely known model of this type. In its original form, the Gurson model deals with an initially spherical void growing in a rigid-perfectly plastic matrix, and assumes that the void remains spherical throughout the entire loading history.

Since then, several extensions have been proposed in order to build more predictive ductile fracture models, along different lines (see also the recent review by Benzerga and Leblond (2010)):

* Corresponding author. Tel.: +32 10 47 24 90; fax: +32 10 47 40 28.
E-mail addresses: liza.lecarme@uclouvain.be (L. Lecarme), thomas.pardoen@uclouvain.be (T. Pardoen).

0749-6419/$ - see front matter © 2011 Elsevier Ltd. All rights reserved.
doi:10.1016/j.ijplas.2011.01.004

- Tvergaard (1981, 1982) introduced tuning parameters, named q_1, q_2 and q_3, into the description of the Gurson yield surface in order to make the model more accurate when compared to FE cell calculations. These fits have been generalized by several authors later, see e.g. Gao et al. (1998). The Gurson model has also been heuristically generalized by Nahshon and Hutchinson (2008) to better account for shear distortion.
- Void nucleation and void coalescence criteria have been added to the Gurson formalism in order to produce a complete model up to final failure, see early works by Chu and Needleman (1980), and Tvergaard and Needleman (1984). Recently, many efforts have been made to improve the description of the void coalescence stage (Benzerga et al., 2004; Fabrègue and Pardoen, 2008; Leblond and Mottet, 2008; Pardoen and Hutchinson, 2000, Scheyvaerts et al., 2010b; Zhang and Niemi, 1995).
- The description of the void geometry has been refined essentially by accounting for the void aspect ratio, assuming spheroidal void shape (Gologanu et al., 1993, 1994, 1997) followed by Benzerga and Besson (2001), Benzerga et al. (2004), Keralavarma and Benzerga (2008), Monchiet et al. (2006, 2008), and Pardoen and Hutchinson (2000). Void rotation has been first treated by Gologanu et al. (1997), and later refined by Scheyvaerts et al. (2011).
- The response of the matrix surrounding the void, starting from perfect J_2 plasticity in the original Gurson, has been improved. First, Gurson (1977b) heuristically introduced strain hardening by replacing the initial yield stress by the current yield stress of the matrix material. This approach was later improved by Leblond et al. (1995) who derived a more accurate formulation for large strain hardening exponents. Kinematic hardening (Besson and Guillemer-Neel, 2003; Mear and Hutchinson, 1985), plastic anisotropy (Keralavarma and Benzerga, 2010; Monchiet et al., 2008), and rate sensitivity (Besson, 2009; Klöcker and Tvergaard, 2003; Lassance et al., 2007) have also been introduced into the Gurson or the Gologanu extension. Void size effect related to strain gradient plasticity has been addressed by Wen et al. (2005). Recently, an attempt has been made to describe the response of composite materials involving void growth by a homogenization model which directly relies on the volume fraction and shape of the second phase particles (Tekoğlu and Pardoen, 2010).

These extensions are most often used together with power law type hardening rules to describe the isotropic strain hardening response without connection to the underlying physical mechanisms. In this paper, the four aspects listed above will be addressed, but with an emphasis on the fourth one.

Physics based models for strain hardening relate to the dislocation mechanisms through the strain hardening rate, $\theta = \partial\tau_y/\partial\gamma$, where τ_y is the yield stress in shear, and γ is the corresponding shear strain (for an extensive review on strain hardening in metals, see Kocks and Mecking (2003) and references therein). Here, the counterpart of θ is used, i.e. $\Theta = \partial\sigma_y/\partial\varepsilon^p_{acc}$, with σ_y the flow stress and ε^p_{acc} the accumulated plastic strain, which can be directly obtained from uniaxial tension or compression experiments. In the course of plastic deformation of a metal, dislocations interact with each other and with obstacles via different mechanisms. Although these interaction mechanisms operate simultaneously at all times during deformation, some of them become more dominant during specific range of deformation. Polycrystals present mainly two different hardening stages, referred to as stage III and stage IV in the literature, see Fig. 1.

During stage III in single phase metals, a competition takes place between forest hardening due to dislocation interactions and accumulation, and dynamic recovery of dislocations, leading to a linear decrease of the hardening rate Θ with increasing stress. The stage III hardening is the basis of the empirical strain hardening law of Voce (1955), which was later provided with a physical foundation based on dislocation arguments by Kocks and Mecking (2003), and Mecking and Kocks (1981). If the linear decrease of the hardening rate in stage III would continue till Θ goes to zero, the flow stress would tend to a steady-state limit, σ_v (see the dashed line in Fig. 1), corresponding to a non-strain-hardening regime where mobile dislocations are generated, stored, then immediately recovered. However, in reality, stage III is interrupted before reaching

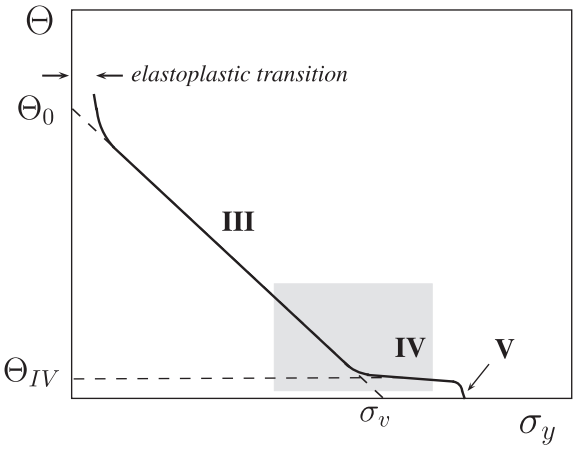

Fig. 1. Evolution of the strain hardening rate Θ with the flow stress σ_y in metallic single phase polycrystals. Θ_0 corresponds to the athermal hardening level, σ_0 to the initial yield stress, and σ_v is the temperature and strain rate dependent Voce stress. The grey rectangle shows the parameter range at which fracture is expected.

the steady-state regime by the so-called stage IV (see e.g. Argon, 2008; Zehetbauer and Seumer, 1993), where $\partial\Theta/\partial\sigma_y \approx 0$, see Fig. 1. The value $\Theta = 0$ may be eventually reached at extremely large strains, due to the occurrence of the so-called stage V, see e.g. Ravi et al. (1980).

In the literature, the process through which Θ goes to zero is either described by a continuously decreasing hardening rate in stage IV, or by a separate stage V, as also shown in Fig. 1. The description of the transition from stage III to stage IV, and from stage IV to stage V, as well as the existence of an independent stage V still lead to open debates in the literature. The transition to stage IV is usually observed at strains on the order of 1 in single crystals (Argon, 2008) but can take place earlier in polycrystals. For instance, Byun et al. (2004) have shown that for a variety of metallic alloys, linear strain hardening is a very good approximation for the evolution of the strength after the onset of necking, which, in their study, was varying widely depending on the material. The occurrence of stage IV hardening at moderate strains (much lower than 1) has also been confirmed recently by Nielsen et al. (2010), and Simar et al. (2010) for Al alloys of the 6xxx series. In this study, it has also been shown that accounting for stage IV was absolutely necessary, not only to predict reliable load displacement responses, but also to allow capturing the evolution of the ductility as a function of the ageing heat treatment. One of the key aspects in these studies was that, in the case of heat treatment leading to low or moderate strengths, void nucleation was taking place late in the deformation process, within stage IV. Hence, the predictions were found to be quite sensitive to the choice of accounting or not for a stage IV and on its magnitude. Stage IV was thus taken into account when modelling the experiments using the Gurson formalism, but without performing any theoretical analysis about the validity of the model coupled to a Kocks-Mecking hardening law. These studies on the fracture of 6xxxx Al alloys have set part of the motivation for the present investigation.

The fracture strain of metals ε_f varies with stress triaxiality T typically in a range from $\varepsilon_f \approx 0.1$ at large stress triaxiality, i.e. $T > 3$, to $\varepsilon_f \geqslant 1$ at low stress triaxiality, i.e. $T < 0.6$ (e.g. during uniaxial tension with necking). Conditions for stage IV hardening are thus definitely attained at low stress triaxiality in terms of the overall deformation. Low stress triaxiality conditions prevail in metal forming applications (Badreddine et al., 2010; Chéhab et al., 2010; Pardoen, 2006) or in thin plate fracture (Pardoen et al., 1999, 2004). Now, even at large stress triaxiality, typical of crack tip regions in thick components (see Pardoen and Hutchinson, 2003; Tvergaard and Hutchinson, 2002), the local strain is likely to reach large values in the close neighborhood of voids, and in the ligaments between closely spaced voids, enough to activate the stage IV hardening. For all these reasons, the significant decrease of the hardening rate during stage III, and the rather abrupt transition from stage III to stage IV, during which the hardening rate is nearly constant, are expected to significantly affect the growth and coalescence of voids. This study has two main objectives:

- The first objective is to analyze to what extent void growth and void coalescence are affected by the details of the stage III and stage IV strain hardening. For this purpose, an extensive parametric study is performed through 2D axisymmetric FE calculations on unit cells containing a spheroidal void at the center. The matrix material of the unit cell is modeled as a J_2 isotropic elasto-plastic solid, with a Kocks–Mecking type strain hardening response. The importance of accounting for the stage IV hardening is emphasized.
- The second objective is to incorporate the Kocks–Mecking strain hardening law into a Gurson type micromechanics based damage model. The damage model uses the Gologanu–Leblond–Devaux (GLD) porous plasticity model for void growth, and a new form of the Thomason void coalescence criterion suitable for a strain hardening matrix. These extensions are important in order to improve the capacity of current ductile failure models to link the physical mechanisms of deformation influenced by the microstructure to the end used fracture properties.

The paper is organized as follows. Section 2 presents the parametric study performed via the unit cell calculations. Section 3 introduces the ingredients of the damage model, that is the GLD porous plasticity and the Thomason void coalescence criterion, which are both modified in order to account for a Kocks–Mecking type strain hardening law. In Section 4, the full damage model is assessed towards the unit cell calculations. Finally, Section 5 concludes this paper.

2. Parametric study

2.1. FE void cell model

The void cell calculations performed in this paper directly follow the methodology set by Koplik and Needleman (1988). A solid material containing regularly distributed voids can be represented by a 3D periodic array of hexagonal cylindrical unit cells, each containing a void at its center. In order to decrease the computational time, the hexagonal cylinders are approximated by circular cylinders, which allow 2D axisymmetric calculations. Even though the circular cylinders do not completely fill the space when stacked together, they provide a good approximation for hexagonal cells, as shown in e.g. Worswick and Pick (1990). Due to the symmetry of the problem, only one quarter of a unit cell is meshed, see Fig. 2. Three non-dimensional parameters related to the unit cell dimensions fully characterize the damage configuration: the void aspect ratio W, the relative void spacing χ, and the porosity f, defined as

$$W = \frac{R_z}{R_r}, \quad \chi = \frac{R_r}{L_r}, \quad f = \frac{2R_r^2 R_z}{3L_r^2 L_z}, \tag{1}$$

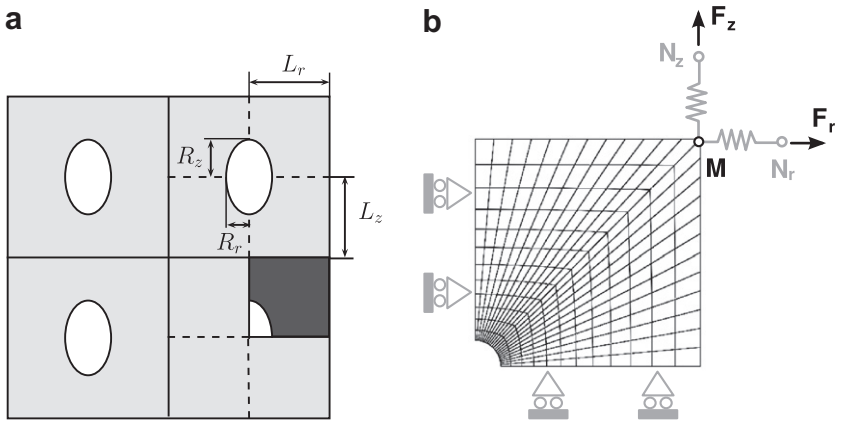

Fig. 2. (a) Geometry and dimensions of the unit cell and (b) a typical mesh with the boundary conditions and the loading system used for axisymmetric tensile calculations under constant stress triaxiality.

where R_r and R_z are, respectively, the radial and axial void radii, and L_r and L_z are respectively the radial and axial mean void spacings, see Fig. 2(a).

The FE calculations are performed within a finite strain setting, using the commercial software ABAQUS, 2008. The logarithmic strain components ε_{rr} and ε_{zz} are directly obtained from the change of the unit cell dimensions, see Fig. 2(a):

$$\varepsilon_{rr} = \ln\left(\frac{L_r}{L_{r0}}\right), \quad \varepsilon_{zz} = \ln\left(\frac{L_z}{L_{z0}}\right). \tag{2}$$

The loading corresponds to axisymmetric tension – with the main loading in the z axis direction – and the stress triaxiality T is kept constant during the entire loading history. In the literature, different methods are used to keep the stress triaxiality constant (see e.g. Brocks et al., 1995; Lin et al., 2006; Pardoen and Hutchinson, 2000; Steglich et al., 2008). Here, the following method is used. An extra node M is created at the top right corner of the cell, see Fig. 2(b). In order to enforce periodicity, the top and side surfaces of the unit cell are kept straight by coupling the displacements in the axial (i.e. the z axis) and radial (i.e. the r axis) directions, respectively, of all the nodes on these surfaces to the corresponding displacements of the node M. Also, for the nodes of the bottom surface (of the axis of symmetry), the axial (the radial) displacements are fixed while imposing zero traction in the radial (the axial) direction. Note that, for the axisymmetric loading condition analysed here, the ratio of the radial tensile stress σ_{rr} to the axial tensile stress σ_{zz} acting on the unit cell is related to the stress triaxiality T through

$$\frac{\sigma_{rr}}{\sigma_{zz}} = \frac{3T-1}{3T+2}. \tag{3}$$

As the displacements of the top and side surfaces of the unit cell are coupled to the displacements of the node M, a point force applied to the node M is fully transmitted to the unit cell, and the stress tractions read

$$\sigma_{rr} = \frac{F_r}{2\pi L_r L_z}, \quad \sigma_{zz} = \frac{F_z}{\pi L_r^2}, \tag{4}$$

where F_r and F_z are, respectively, the radial and axial forces acting on the node M. To apply these forces, two additional nodes are created, N_r and N_z, which are connected to the node M via two springs (CONN2D2 elements of the ABAQUS element library), see Fig. 2(b). Now, the point forces read

$$F_r = c\left(u_r^{N_r} - u_r^M\right), \quad F_z = c\left(u_z^{N_z} - u_z^M\right), \tag{5}$$

where u_r and u_z are, respectively, the radial and axial displacements, and c is the stiffness of the springs. Inserting Eqs. (4) and (5) into Eq. (3), a single equation with four unknowns is obtained which needs to be satisfied at each strain increment to keep the stress triaxiality T constant:

$$-\left(u_r^{N_r} - u_r^M\right)L_r + 2\left(u_z^{N_z} - u_z^M\right)L_z\frac{3T-1}{3T+2} = 0. \tag{6}$$

In order to solve Eq.(6), an ABAQUS user subroutine to define multi-point constraints is used (see MPC subroutine in ABAQUS, 2008).

Axisymmetric, four-noded, bilinear elements (CAX4 elements of the ABAQUS element library) are used for the mesh, and detailed convergence studies have been performed to ensure that the results are independent of the mesh refinement up to after the onset of void coalescence. The matrix of the unit cell is modeled as an isotropic J_2 elastoplastic material with the

hardening law given in a pointwise manner based on the Kocks–Mecking model, see the next section. The method used in this paper to keep the stress triaxiality constant is very successful and computationally more efficient compared to other iterative methods employed in earlier works (see e.g. Pardoen and Hutchinson (2000)) and more accurate than the Riks approach (Lassance et al., 2006; Steglich et al., 2008). The convergence of the results is independent from the stiffness of the springs, c, but the larger the stiffness, the faster the calculations are performed. Yet, the internal iterations of the ABAQUS solver for the MPC subroutine do not converge for very large c values; a value of $c \approx 50EL_{r0}$ is used, with E being the Young's modulus of the matrix of the unit cell and L_{r0} being the initial radial mean void spacing for the unit cell set equal to 1, see Fig. 2.

Voids grow with the plastic deformation of the surrounding matrix, and the relative distance between neighboring voids, χ, decreases. At some point, plastic deformation localizes inside the ligaments connecting neighboring voids, while the rest of the unit cell goes through elastic unloading, see Fig. 3. This point corresponds to the onset of void coalescence, after which the unit cell deforms in a uniaxial straining mode, i.e. with $|\partial\varepsilon_{rr}/\partial\varepsilon_{zz}|$ becoming very small. The onset of coalescence is considered to occur when $|\partial\varepsilon_{rr}/\partial\varepsilon_{zz}|$ becomes smaller than 5% of its value during the first part of the deformation. The transition being very sharp, the selected magnitude of the change of slope has almost no effect on the determination of the coalescence strain. In the present axisymmetric problem, the localization sets in the ligament perpendicular to the main loading direction – which is aligned with the z-axis, see Fig. 2 – leading to the so-called internal necking mode of coalescence.

2.2. Strain hardening model

A Kocks–Mecking type hardening law is used, which explicitly accounts for stages III and IV, for the strain hardening of the unit cell matrix. Stage III is approximated by a linear decrease of the hardening rate with a constant slope β, i.e. $\partial\Theta/\partial\sigma_y = -\beta$, and stage IV by a constant hardening rate, $\Theta = \Theta_{IV}$, see Fig. 4. Even though the transition from stage III to stage IV is smoother in reality, see e.g. Simar et al. (2010), a sharp transition is assumed here, in order to limit the number of parameters in the model. In the integrated form, the Kocks–Mecking hardening law reads

$$\sigma_y = \begin{cases} \sigma_0 + \frac{\Theta_0}{\beta}\left[1 - \exp(-\beta\varepsilon^p_{acc})\right] & \text{for } \sigma_y \leqslant \sigma_y^{\mathrm{tr}} \quad \text{(stage III)}, \\ \sigma_y^{\mathrm{tr}} + \Theta_{IV}\left(\varepsilon^p_{acc} - \varepsilon^{p\_\mathrm{tr}}_{acc}\right) & \text{for } \sigma_y > \sigma_y^{\mathrm{tr}} \quad \text{(stage IV)}, \end{cases} \tag{7}$$

where σ_0 is the initial yield stress, and σ_y^{tr} and $\varepsilon^{p\_\mathrm{tr}}_{acc}$ correspond, respectively, to the values of the flow stress and of the accumulated plastic strain at the transition point from stage III to stage IV, given as

$$\sigma_y^{\mathrm{tr}} = \sigma_0 + \frac{\Theta_0 - \Theta_{IV}}{\beta}, \tag{8}$$

$$\varepsilon^{p\_\mathrm{tr}}_{acc} = \frac{1}{\beta}\ln\left(\frac{\Theta_0}{\Theta_{IV}}\right). \tag{9}$$

2.3. Results of the parametric study

Before presenting the results of the parametric study, it is important to underline the physical relevance of the material properties used in the rest of the paper, for the unit cell calculations as well as for the parametric studies performed later

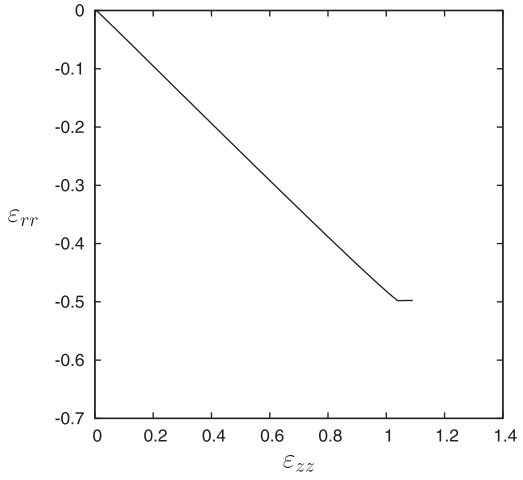

Fig. 3. Evolution of the radial strain ε_{rr} with axial strain ε_{zz}, with $T = 1$, $W_0 = 1$, $\Theta_0/\sigma_0 = 10$, $\beta = 15$ and $\Theta_{IV} = 1$. The sharp change in slope indicates the onset of coalescence, with $|\partial\varepsilon_{rr}/\partial\varepsilon_{zz}|$ becoming smaller than 5% of its value during the first part of the deformation.

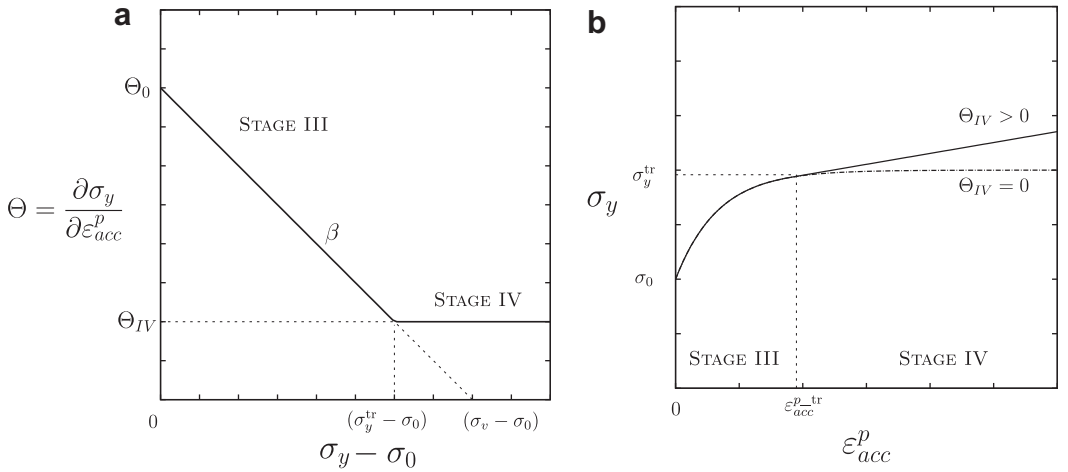

Fig. 4. Schematic representation of the Kocks–Mecking type strain hardening law used in this paper. (a) Stage III is represented by a linear decrease of the hardening rate with a constant slope β, i.e. $\partial\Theta/\partial\sigma_y = -\beta$, and stage IV is approximated by a constant hardening rate, $\Theta = \Theta_{IV}$. (b) Corresponding yield stress-accumulated plastic strain curve showing the cases $\Theta_{IV} = 0$ (no stage IV) and $\Theta_{IV} > 0$.

with the damage model, see Table A.1. The material properties have been chosen to encompass a large range of parameters typical of aluminum alloys, involving various precipitation hardening conditions, see e.g. Simar et al. (2007). Several authors observed that, for single crystals under uniaxial tension, stage IV usually starts at very large strains over 1, well after the onset of necking that corresponds to the Considère point with $\Theta = \sigma_y$, see e.g. Argon (2008), and Rauch (2009). Now, for a wide range of polycrystalline metals, the strain hardening rate Θ remains, to a very good approximation, constant after the Considère point, see e.g. Byun et al. (2004), and Nielsen et al. (2010) as well as the short discussion in the introduction. The values of the parameter Θ_{IV} were thus chosen to vary widely between 0 (i.e. no stage IV), and the Considère stress, $\sigma_u = (\beta\ \sigma_0 + \Theta_0)/(1 + \beta)$.

2.3.1. Influence of T and W_0, with or without stage IV hardening

Fig. 5 shows the variation of (a,b) the axial stress σ_{zz}, (c,d) the porosity f, and (e,f) the void aspect ratio W as a function of the axial strain ε_{zz}, for (a,c,e) three different stress triaxiality values, $T = 2/3$, 1, 3, with $W_0 = 1$, and for (b,d,f) three different initial void aspect ratio values, $W_0 = 1/3$, 1, 3, with $T = 1$. Two cases are presented in each figure: $\Theta_{IV} = 0$ with dashed lines and $\Theta_{IV} = \sigma_u$ with solid lines. For $\Theta_{IV} = 0$, the strain hardening is entirely dictated by the stage III response (with $\Theta_0/\sigma_0 = 3$, and $\beta = 15$), and the strain hardening rate Θ linearly decreases down to zero with increasing stress. For $\Theta_{IV} = \sigma_u$, on the other hand, the strain hardening is governed by stage III until the Considère point $\Theta = \sigma_y$, and by stage IV afterwards. The onset of void coalescence is indicated by a filled circle • on each curve. The results are shown only for the calculations with an initial porosity $f_0 = 0.1\%$, but similar tendencies are observed for other f_0 values.

The results for $\Theta_{IV} = 0$, i.e. only stage III hardening, closely resemble the results obtained in the literature for a power law with a strain hardening exponent $n \simeq 0.1$, see e.g. Koplik and Needleman (1988), and Pardoen and Hutchinson (2000). An important difference between the two cases $\Theta_{IV} = 0$ and $\Theta_{IV} = \sigma_u$ is that, for the former, a distinct softening regime is observed after the peak stress before the onset of void coalescence, while, for the latter, void coalescence initiates soon after the peak stress is reached, as shown in Figs. 5(a) and (b). As expected, void coalescence occurs earlier with increasing stress triaxiality T, irrespective of the strain hardening behavior of the matrix material. Note also that coalescence was not attained for $T = 2/3$ in either case of strain hardening. Fig. 5(b) shows that the more prolate the initial void is, the later void

Table A.1
Material properties used for the unit cell calculations and the damage model.

Parameter	Name	Value (s)
E	Young's modulus	70 000 MPa
ν	Poisson ratio	0.3
σ_0	Initial yield stress	300 MPa
f_0	Initial porosity	0.1%
T	Stress triaxiality	0.66, 1, 1.5, 2, 3
W_0	Initial void aspect ratio	0.33, 1, 3
β	Dynamic recovery rate	2.5, 5, 8, 12, 15, 20, 40, 50
Θ_0/σ_0	Normalized dislocation storage rate	2, 3, 10, 20
Θ_{IV}/σ_0	Normalized stage IV hardening rate	0, 0.4, 0.7, 1, σ_u/σ_0

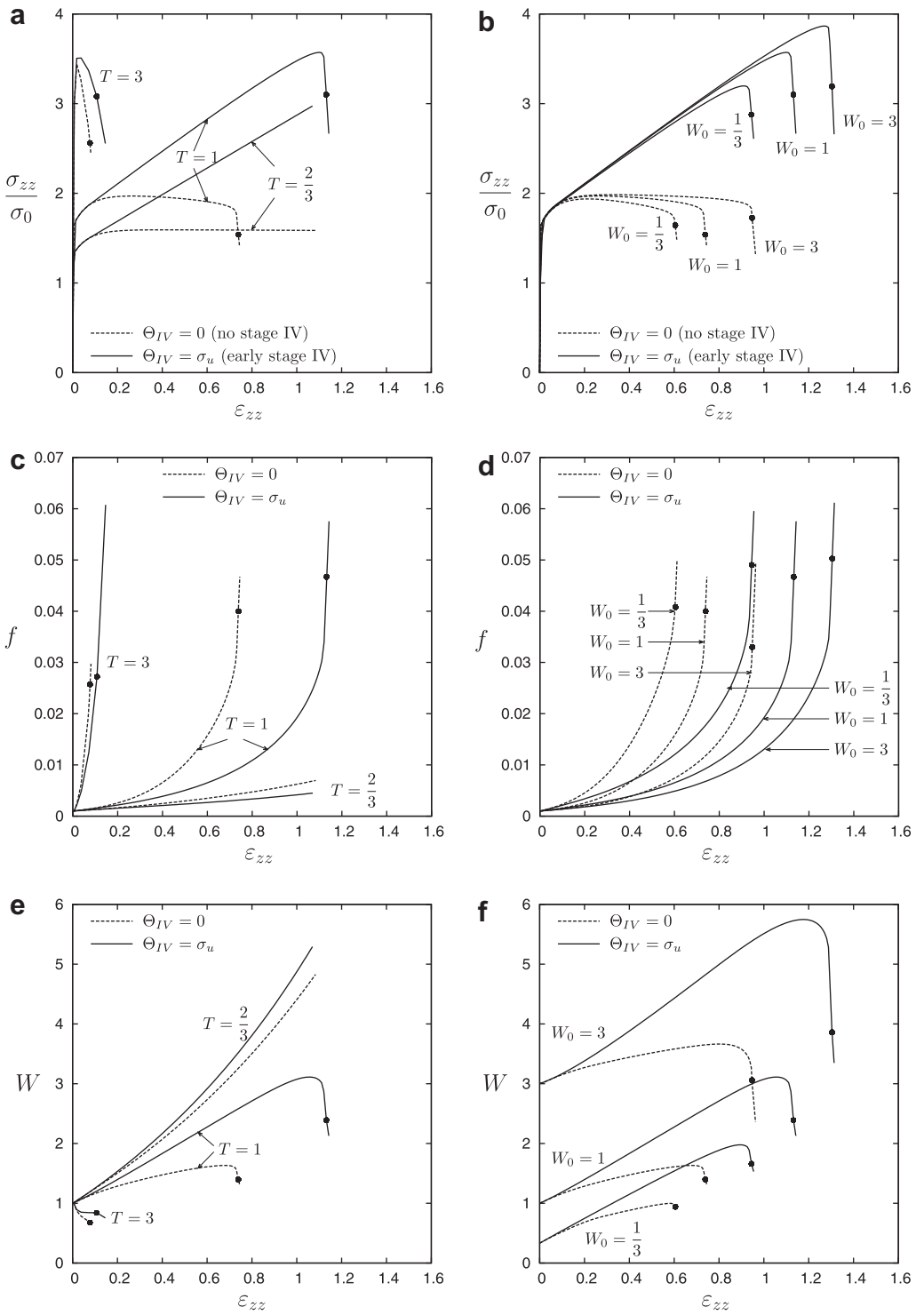

Fig. 5. Variation of the (a,b) axial stress σ_{zz}, (c,d) porosity f, and (e,f) void aspect ratio W as a function of the axial strain ε_{zz}, for (a,c,e) different values of stress triaxiality T, with $W_0 = 1$, and for (b,d,f) different values of the initial void aspect ratio values W_0, with $T = 1$. Dashed lines correspond to $\Theta_{IV} = 0$, i.e. only stage III hardening (with $\Theta_0/\sigma_0 = 3$ and $\beta = 15$), and solid lines to $\Theta_{IV} = \sigma_u$, i.e. both stages III and IV hardening. The onset of void coalescence is indicated by a filled circle •.

coalescence sets in, see also Pardoen and Hutchinson (2000). For low porosity, as investigated here, the void aspect ratio has only a very limited effect on the overall stress evolution and affects only the onset of coalescence.

The porosity increases faster for $\Theta_{IV} = 0$, the effect being more pronounced at low and moderate stress triaxialities, see Figs. 5(c) and (d). Fig. 5(d) also shows that voids grow faster when they are initially oblate ($W_0 < 1$) than when initially prolate ($W_0 > 1$). The difference in the void growth rate for different Θ_{IV} values appears already at relatively small strain values. In fact, for $\Theta_{IV} = \sigma_u$, the transition from stage III to stage IV occurs early in the deformation process, at the close vicinity of the void where large local strain values are reached at rather low overall strains. After the transition, the strain hardening capacity is obviously larger for the case $\Theta_{IV} = \sigma_u$ than for $\Theta_{IV} = 0$, which makes void growth more difficult. Fig. 6 shows two contour plots of equivalent plastic strain, ε^p_{eq}, for $T = 1$, $W_0 = 1$, $\Theta_0/\sigma_0 = 10$, for (a) $\Theta_{IV} = 0$, and (b) $\Theta_{IV} = \sigma_u$, at an overall axial strain value $\varepsilon_{zz} = 0.6$, which is before the onset of coalescence; the local strain around the void is larger for (a), for which case the void growth rate is also larger. Plastic flow is also more localized in the absence of stage IV ($\Theta_{IV} = 0$) due to the absence of strain hardening (perfect plasticity) at large strains.

Finally, Figs. 5(e) and (f) show that for low and moderate stress triaxiality and for all initial void aspect ratio values, voids have a tendency to become more prolate for $\Theta_{IV} = \sigma_u$ than for $\Theta_{IV} = 0$. For $T = 3$, however, voids deform toward an oblate shape for either case. Indeed, for $T = 3$, void coalescence initiates at a very low overall strain value, which does not allow distinguishing the differences related to different strain hardening mechanisms.

2.3.2. Influence of the strain hardening parameters Θ_0, Θ_{IV} and β

Fig. 7 shows the variation of the (a,b) axial stress σ_{zz}, (c,d) porosity f, (e,f) void aspect ratio W as a function of the axial strain ε_{zz}, for different values of (a,c,e) Θ_0, and (b,d,f) Θ_{IV}; for (a,c,e), $\Theta_{IV} = 0$, and for (b,d,f) $\Theta_0 = 10\sigma_0$, with $T = 1$, $W_0 = 1$, $\beta = 15$ for all the calculations. For $\Theta_{IV} = 0$, the peak stress, which increases with increasing Θ_0, is reached relatively early, while for $\Theta_{IV} > 0$ it is postponed until soon before the onset of void coalescence, see Figs. 7(a) and (b). During deformation of the unit cell, there is a competition between the hardening due to strain hardening of the matrix material, and softening due the increase of porosity, as can be observed from the stress–strain curves. Even for a relatively low Θ_{IV} value, the strain hardening of the matrix dominates almost throughout the entire deformation regime, see Fig. 7(b). For $\Theta_{IV} = 0$, although Θ_0 controls the value of the peak stress, it has almost no effect either on the void growth rate, see Fig. 7(c), or on the evolution of the void aspect ratio, see Fig. 7(e). Consequently, the strain value corresponding to the onset of void coalescence is almost the same for all Θ_0 values. With increasing Θ_{IV}, however, the void growth rate decreases, see Fig. 7(d), and voids have a tendency to become more prolate, see Fig. 7(f), which postpones the onset of coalescence. Note also that the slope of the unloading curve after the onset of coalescence is hardly affected by the value of Θ_{IV}, as evident from the initial part of the unloading curves shown in the stress–strain figures.

In contrast with the athermal hardening rate Θ_0, the dynamic recovery rate β has a strong effect on the void growth and void aspect ratio evolution rates, depending on the value of the stage IV hardening rate Θ_{IV}, see Fig. 8. With increasing β (i.e. with increasing rate of reduction of Θ, see Fig. 4), the void growth rate increases and void coalescence starts earlier if $\Theta_{IV} = 0$, i.e. only stage III hardening, see Figs. 8(a) and (c). The rate of change of void aspect ratio also decreases with increasing β and voids become less prolate, see Fig. 8(e). On the other hand, if $\Theta_{IV}/\sigma_0 = 1.5$, the tendency is inversed: void coalescence starts later, and voids grow slower and become more prolate with increasing β, see Figs. 8(b), (d) and (f).

Finally, Fig. 9 shows the variation of the axial strain at the onset of void coalescence, ε^c_{zz}, as a function of the normalized stage IV hardening rate, Θ_{IV}/σ_0, for several values of the dynamic recovery rate β. The plastic strain at the onset of void coalescence is a good approximation of the true local fracture strain corresponding to the end of the coalescence process,

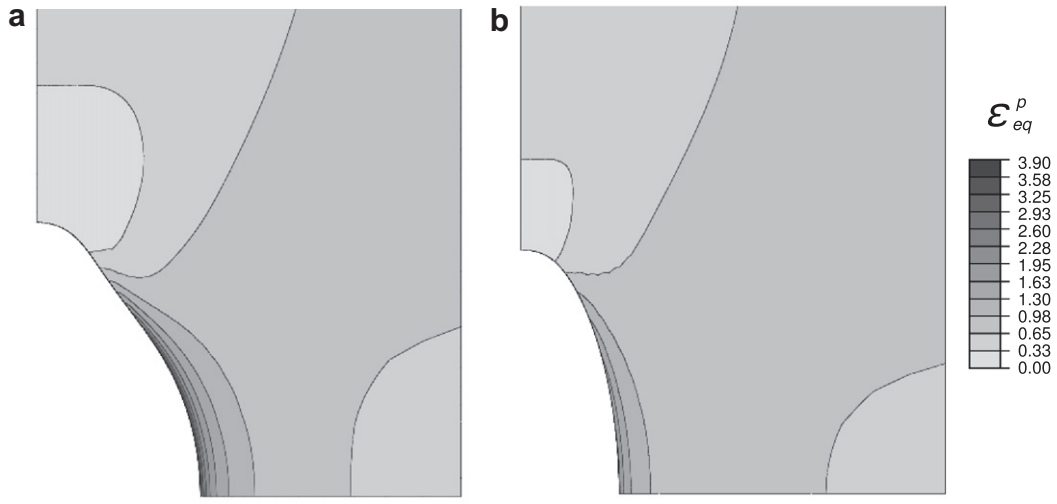

Fig. 6. Contour plots of the local equivalent plastic strain ε^p_{eq} in the region close to the void for (a) $\Theta_{IV} = 0$, (b) $\Theta_{IV} = \sigma_u$, at an overall axial strain value $\varepsilon_{zz} = 0.6$, for $T = 1$, $W_0 = 1$, $\Theta_0/\sigma_0 = 10$ and $\beta = 15$.

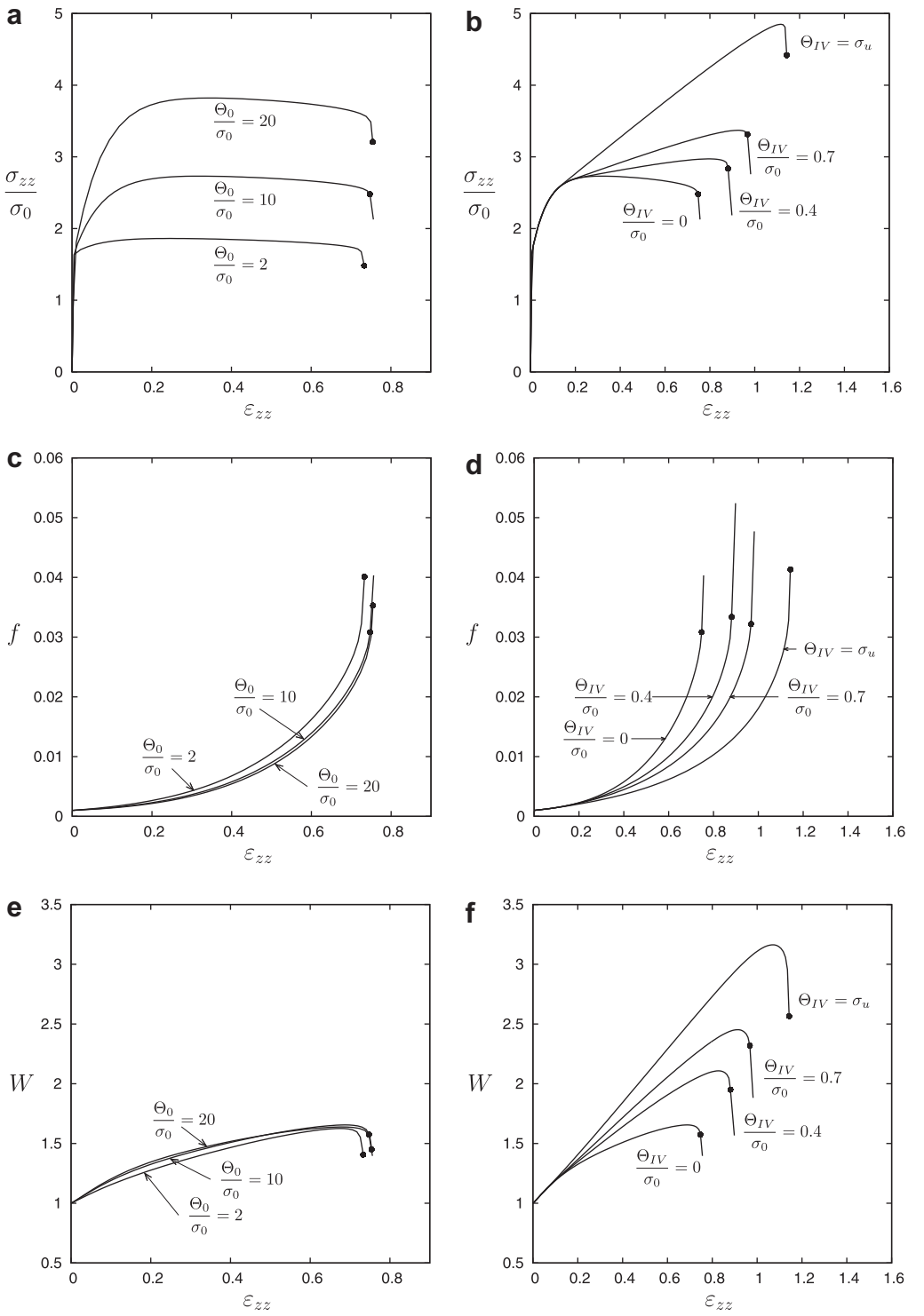

Fig. 7. Variation of the (a,b) axial stress σ_{zz}, (c,d) porosity f, (e,f) void aspect ratio W as a function of the axial strain ε_{zz}, for different values of (a,c,e) Θ_0, and (b,d,f) Θ_{IV}; for (a,c,e), $\Theta_{IV} = 0$, for (b,d,f) $\Theta_0 = 10\sigma_0$, and $T = 1$, $W_0 = 1$, $\beta = 15$ for all the calculations. The onset of void coalescence is indicated by a filled circle •.

see Pardoen and Brechet (2004), and Simar et al. (2010). As also shown in Fig. 7, void coalescence is postponed with increasing Θ_{IV}, but this effect is less obvious for low β values. Furthermore, the influence of β on ε_{zz}^c strongly depends on the value of Θ_{IV}: for $\Theta_{IV}/\sigma_0 \lesssim 0.7$, ε_{zz}^c decreases with increasing β, whereas for larger Θ_{IV} values an opposite tendency is observed, i.e.

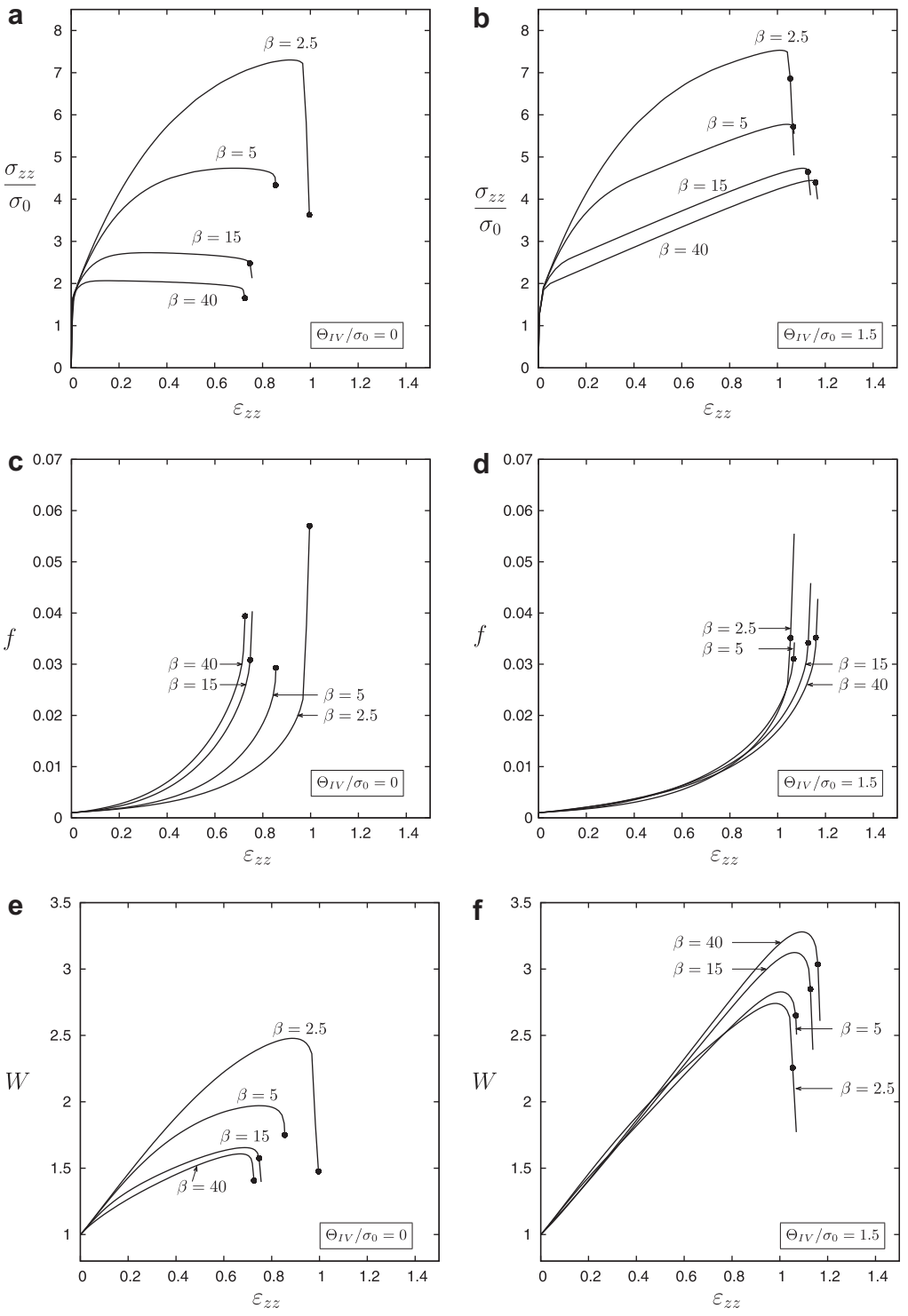

Fig. 8. Variation of the (a,b) axial stress σ_{zz}, (c,d) porosity f, and (e,f) void aspect ratio W as a function of the axial strain ε_{zz}, for different values of the dynamic recovery rate β, with (a,c,e) $\Theta_{IV}/\sigma_0 = 0$, (b,d,f) $\Theta_{IV}/\sigma_0 = 1.5$, and $T = 1$, $W_0 = 1$, $\Theta_0/\sigma_0 = 10$ for all the calculations. The onset of void coalescence is indicated by a filled circle •.

ε^c_{zz} increases with increasing β. Indeed, at large Θ_{IV}, reaching stage IV earlier, as allowed by a higher β, is similar to produce, on average, a higher strain hardening capacity. A high strain hardening capacity delays void growth and the onset of coalescence. The same reason applies to low Θ_{IV}, where the best way to keep a high strain hardening capacity is to have a low β.

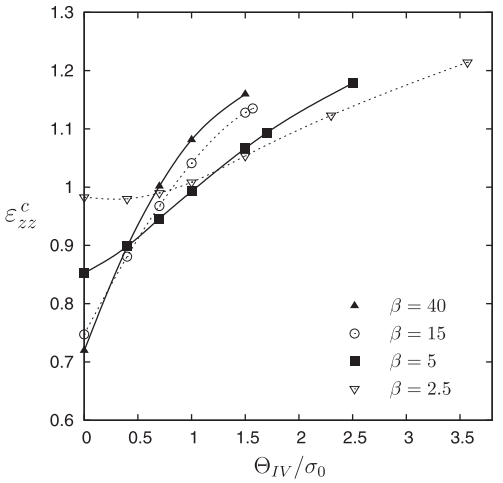

Fig. 9. Variation of the axial strain at coalescence ε^c_{zz} with the normalized stage IV parameter Θ_{IV}/σ_0, for different values of the dynamic recovery rate β, with $T = 1$, $W_0 = 1$, $\Theta_0/\sigma_0 = 10$.

3. Damage model

3.1. The Gologanu–Leblond–Devaux void growth model

Voids continuously grow and change shape with increasing plastic deformation of the surrounding matrix material. When imposing volume conservation of the matrix, the void growth rate in a ductile solid reads

$$\dot{f} = (1-f)\dot{\varepsilon}^p_{ii}, \quad (i = r, \theta, z). \tag{10}$$

As stated earlier in the introduction section, the original Gurson model deals with the growth of a spherical void. Gologanu et al., 1993, 1994, 1997 extended the Gurson model to account for spheroidal void shapes. In the Gologanu–Leblond–Devaux (GLD) model, for the axisymmetric loading conditions analyzed in this paper – for which the main void axis remains parallel to the maximum principal stress – the evolution of the void aspect ratio reads

$$\frac{\dot{W}}{W} = (1 + h_S h_T h_f)(\dot{\varepsilon}_{zz} - \dot{\varepsilon}_{rr}) + h_{Sf}\dot{\varepsilon}_{ii}, \tag{11}$$

where the correction factor h_S is a function of the void shape W, h_f is a function of the porosity f, and h_{Sf} is a function of both W and f. Expressions for these dummy parameters can be found in Gologanu et al. (1993, 1994, 1997) or Lassance et al. (2007). Note also that the parameter h_T is a polynomial function of stress triaxiality T and depends on strain hardening; it has been adjusted by Pardoen and Hutchinson (2000) for a power law hardening description of the form

$$\sigma_y = \sigma_0\left(1 + \frac{E}{\sigma_0}\varepsilon^p_{acc}\right)^n. \tag{12}$$

The plastic strain $\dot{\varepsilon}^p_{ij}$ is normal to the flow potential Φ

$$\dot{\varepsilon}^p_{ij} = \dot{\gamma}\frac{\partial \Phi}{\partial \sigma_{ij}}, \tag{13}$$

and Φ is given as

$$\Phi = \frac{C}{\sigma_y^2}\left(\sigma_{zz} - \sigma_{rr} + \eta\sigma^g_h\right)^2 + 2q(g+1)(g+f)\cosh\left(\kappa\frac{\sigma^g_h}{\sigma_y}\right) - (g+1)^2 - q^2(g+f)^2 = 0, \tag{14}$$

where

- C, η, g, κ and α_2 are analytical functions of W and f, see e.g. Gologanu et al. (1993, 1994, 1997), Lassance et al. (2007), and Pardoen and Hutchinson (2000).
- σ^g_h is a generalized hydrostatic stress defined as: $\sigma^g_h = 2\alpha_2\sigma_{rr} + (1 - 2\alpha_2)\sigma_{zz}$.
- q is a calibration parameter which depends on strain hardening. Similar to the parameter h_T, q has been adjusted by Pardoen and Hutchinson (2000), and Lassance et al. (2007) for the power law strain hardening given by Eq. (12), see further.

The accumulated plastic strain rate $\dot{\varepsilon}^p_{acc}$ is determined from the energy balance initially proposed by Gurson (1977a)

$$\sigma_y \dot{\varepsilon}^p_{acc}(1-f) = \sigma_{ij}\dot{\varepsilon}^p_{ij} \tag{15}$$

and the evolution of the flow stress σ_y is directly given by the Kocks–Mecking strain hardening relationship, Eq. (7). Finally, $\dot{\sigma}_y$ is given by the consistency condition

$$\dot{\Phi}(\sigma_y, \sigma_{ij}, f, W) = 0. \tag{16}$$

The original GLD model is an upper-bound limit load solution for a spheroidal void growing in a rigid-perfectly plastic matrix. It has been later heuristically extended by Pardoen and Hutchinson (2000) to account for the power law strain hardening given by Eq. (12). Here, the GLD model is extended for the Kocks–Mecking hardening law given by Eq. (7). Only two parameters, q and h_T, are related to the strain hardening; therefore only these two parameters must be adapted to the Kocks–Mecking hardening law.

3.1.1. New calibration of the parameter q

The heuristic parameter q as initially introduced by Tvergaard (1981, 1982)[1] in Eq. (14) has been adjusted by Pardoen and Hutchinson (2000) by comparing the predictions of the GLD model with the results of unit cell calculations, similar to those performed in this paper, with the objective of getting the best agreement in the early stage of deformation. For the parameter q, the following expression was suggested

$$q = \frac{1}{2} + q_1 \left| \frac{q_b - 1}{\pi} \right| + \frac{1}{2} q_b, \tag{17}$$

where $q_1 = \arctan(10 - 4T)$. In order to avoid introducing a dependence on the stress triaxiality T, q_1 is taken here as equal to 1.5, as also proposed by Lassance et al. (2007). The parameter q_b, which is a function of f_0, W_0 and n, is given as

$$q_b = 1 + \left(f_{sh} - \frac{1}{2} f_0^{\frac{1}{4}} \right) \left(\frac{1}{2} + \frac{\arctan(2.4 - 2\ln W_0)}{\pi} - \frac{1}{44 W_0} \right) \tag{18}$$

with

$$f_{sh} = 0.65 - 1.75n. \tag{19}$$

Note that Eq. (18) is valid for $W_0 > 0.1$; for $W_0 < 0.1$, q_b is taken to be equal to $q_b(f_0, n, W_0 = 0.1)$, see Lassance et al. (2007). The validity of (19) has been checked in the range $n = 0.1$ to 0.3 (Pardoen and Hutchinson, 2000).

Now, the strain hardening exponent corresponding to the hardening law (7) is not a constant. Fig. 10 shows the evolution of the incremental strain hardening exponent $\partial(\ln \sigma)/\partial(\ln \varepsilon^p)$, called here n_ε. For a power law description, n_ε is constant, equal to n. During straining, n_ε increases very fast from zero to a maximum value n^*_ε and then decreases. If the strain hardening capacity of the material involves a stage IV, n_ε increases again after $\varepsilon^{p\_tr}_{acc}$ has been reached. The higher the value of Θ_{IV}, the earlier stage IV starts and the larger the increase of n_ε with strain. If there is no stage IV, i.e. $\Theta_{IV} = 0$, n_ε keeps decreasing slowly with deformation to asymptotically tend to zero. A simple extension of the definition of f_{sh} in Eq. (19) in the case of a varying strain hardening exponent is to calculate the incremental value n_ε and introduce an evolving $f_{sh}(n_\varepsilon)$:

$$f_{sh}(n_\varepsilon) = 0.65 - 1.75 n_\varepsilon. \tag{20}$$

An alternative approach to re-express f_{sh}, based on β and Θ_{IV}, is proposed in Appendix.

3.1.2. New calibration of the parameter h_T

In the work of Gologanu et al. (1997), h_T is defined as a polynomial function of T, to give the best agreement between the void shape evolution predicted by Eq. (11) and the (as) exact (as possible) numerical solution given by the FE cell calculations. Pardoen and Hutchinson (2000) provide two different expressions, according to the value of the strain hardening exponent n equal to 0.1 or 0.3, when expressed with a power law as (12). The values of h_T for intermediate n can be obtained by linear interpolation.

Same as for f_{sh}, the h_T parameter is adjusted as a function of n_ε. Here, the method of Pardoen and Hutchinson (2000) has not been followed; a new, more accurate fit is proposed. The void shape evolution has been fitted in the early stages of deformation, based on a large number of cell calculations performed using the Kocks–Mecking hardening law in the following way. A single constant h_T value has been first determined to best match the beginning of the evolution of W with straining. This value of h_T is associated to the peak n^*_ε, which is an upper bound approximation of the mean n_ε during the first stages of deformation. This is done for a wide set of parameters $(T, \beta, \Theta_0, \Theta_{IV})$, while the following $f_0 = 0.1\%$ and $W_0 = 1$ have been kept constant. Fig. 11 exhibits the values of the best h_T obtained from the model and adjusted to the cell calculations for different n^*_ε and stress triaxialities T. For each value of T, a polynomial function of $h_T(n^*_\varepsilon)$ fitting the results is found. Moreover, for each value of n^*_ε, h_T can also be expressed as a polynomial function of T (not shown). Now, in order to account for the fact that n_ε

[1] As a matter of fact, Tvergaard introduced three parameters q_1, q_2 and q_3; q_3 being equal to q_1^2. The parameter q_2 was essentially correcting for the absence of void shape effects in the original Gurson formalism but is not necessary anymore in the formalism of the GLD model.

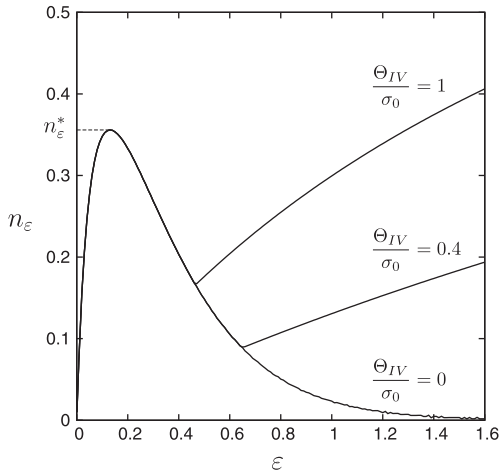

Fig. 10. Evolution of the incremental strain hardening exponent n_ε^* with strain, using: $T = 1$, $W_0 = 1$, $\Theta_0/\sigma_0 = 10$, $\beta = 5$.

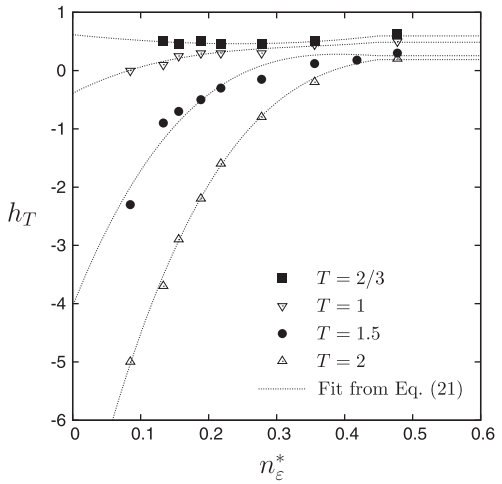

Fig. 11. Evolution of the h_T parameter with strain hardening exponent maximum value n_ε^* and stress triaxiality T, using: $W_0 = 1$.

varies with strain, the expression found for various n_ε^* in the early stages of deformation, i.e. $h_T(n_\varepsilon^*)$ is changed all along deformation, i.e. n_ε^* is replaced by the current n_ε in h_T. A more rigorous procedure based on an exact average n_ε over the range of strains used for the fitting has been attempted, giving essentially the same result. The generic expression for h_T as a function of both T and n_ε writes

$$h_T = A(n_\varepsilon) + B(n_\varepsilon)T + C(n_\varepsilon)T^2 + D(n_\varepsilon)T^3, \tag{21}$$

with

$$A(n_\varepsilon) = 1.69 - 12.50n_\varepsilon + 36.20n_\varepsilon^2 - 28.06n_\varepsilon^3, \tag{22}$$
$$B(n_\varepsilon) = -1.60 + 19.06n_\varepsilon - 59.10n_\varepsilon^2 + 50.20n_\varepsilon^3, \tag{23}$$
$$C(n_\varepsilon) = 0.81 - 7.27n_\varepsilon + 17.71n_\varepsilon^2 - 11.43n_\varepsilon^3, \tag{24}$$
$$D(n_\varepsilon) = -1.29 + 6.62n_\varepsilon - 10.31n_\varepsilon^2 + 4.17n_\varepsilon^3. \tag{25}$$

These expressions are valid for $n_\varepsilon \leqslant 0.45$. When $n_\varepsilon > 0.45$, h_T is taken equal to $h_T(n_\varepsilon = 0.45)$.

3.2. The Thomason void coalescence criterion

During void growth, although strain concentrates in the close vicinity of the voids, plastic deformation spreads throughout the entire matrix material. At some point, the stable growth of voids is interrupted by a uniaxial deformation mode, where plasticity localizes in the ligaments connecting neighboring voids, and the regions off the localization plane undergo

elastic unloading. This sudden transition to localized plasticity is referred to as the onset of void coalescence, i.e. the starting point of the coalescence stage of ductile fracture. For the void distribution and loading conditions analyzed in this paper (see Fig. 2), the only mode of void coalescence which has been observed is the one referred to as *internal necking*, where the ligament between the two voids shrinks in a similar way to the necking process under uniaxial tension. Depending on the void distribution and loading conditions, other modes such as shear and necklace coalescence are also possible, see e.g. Benzerga (2000), Leblond and Mottet (2008). For many metals, the strain increment from the onset of void coalescence to the complete fracture of a sample is only a few percent. Therefore, for practical purposes, approximating the fracture strain of a metal by the strain at the onset of void coalescence provides acceptable accuracy, see Simar et al. (2010).

Thomason (1985, 1990) formulated a condition for the (localized flow) internal necking mode of void coalescence for a rigid-perfectly plastic material:

$$A_l C_f \sigma_0 = A_s \sigma_{zz}, \tag{26}$$

where, for the void distribution and loading condition shown in Fig. 2, A_l is the area of the cross-section containing the ligament connecting the voids, C_f is a coefficient which measures the change in the load carrying capacity of the cross-section A_l due to the presence of a void in the localized flow regime, σ_0 is the yield stress of the matrix material (no strain hardening), A_s is the total surface of the unit cell, and σ_{zz} is the stress applied on A_s. For the coefficient C_f, Thomason proposed, based on fitting slip line solutions, an empirical expression, which, in the notation used in the present paper, reads

$$C_f = \left[\alpha\left(\frac{1-\chi}{\chi W}\right)^2 + \kappa\frac{1}{\sqrt{\chi}}\right], \tag{27}$$

stating also that using $\alpha = 0.1$ and $\kappa = 1.2$ gives the best agreement for a wide range of intervoid matrix geometries. For the axisymmetric unit cell shown in Fig. 2, Eq. (26) reduces to

$$\sigma_{zz} = \sigma_0(1-\chi^2)\left[0.1\left(\frac{1-\chi}{\chi W}\right)^2 + 1.2\frac{1}{\sqrt{\chi}}\right]. \tag{28}$$

Eq. (28) states thus that void coalescence starts when σ_{zz} reaches a critical value set by the right hand side of the equation. This critical value decreases as the voids open (W increases) and get closer to each other (χ increases). Porosity f affects void coalescence indirectly through the softening that it imposes on the applied stress σ_{zz}, as well as through its link with the void spacing and the void aspect ratio; for example, $f = (2/3)W\chi^3/\lambda$, with $\lambda = L_z/L_r$, for the regular void distribution shown in Fig. 2.

In order to adapt the original Thomason criterion to the more realistic case of strain hardening materials, Zhang and Niemi (1995) proposed to replace the initial yield stress, σ_0, by the current overall yield stress of the matrix, σ_y, which can be calculated using the energy balance given in Eq. (15). For the power law strain hardening rule given in Eq. (12), Pardoen and Hutchinson (2000) showed that Eq. (28) accurately predicts the onset of void coalescence when σ_0 is replaced with σ_y, if the parameter α is taken to be a function of the strain hardening exponent, $\alpha(n) = 0.1 + 0.217n + 4.83n^2$, with $0 \leqslant n \leqslant 0.3$, and $\kappa = 1.24$. Again, a simple extension of that idea in the case of a varying strain hardening exponent is to calculate the incremental value n_ε and introduce an evolving $\alpha(n_\varepsilon)$ as

$$\frac{\sigma_{zz}}{\sigma_y} = (1-\chi^2)\left[\alpha(n_\varepsilon)\left(\frac{1-\chi}{\chi W}\right)^2 + 1.24\frac{1}{\sqrt{\chi}}\right]. \tag{29}$$

This will be referred hereafter as the *version 1* of the Thomason model.

3.2.1. New extension of the Thomason criterion for strain hardening materials

In order to avoid the hardening law dependence of the Thomason criterion, Fabrègue and Pardoen (2008), Scheyvaerts et al. (2011) proposed an alternative form

$$\frac{\sigma_{zz}}{\sigma_y^{loc}} = (1-\chi^2)\left[0.1\left(\frac{1-\chi}{\chi W}\right)^2 + 1.24\frac{1}{\sqrt{\chi}}\right], \tag{30}$$

where σ_y^{loc} is the current yield stress next to the void surface, which corresponds to the location of the largest accumulated plastic strain, therefore to the largest local yield stress in the localization plane. In this new form, α is a constant, and the void coalescence criterion is independent of the strain hardening rule used for the matrix material. The local yield stress σ_y^{loc} is related to the local accumulated plastic strain $\varepsilon_{acc}^{p\_loc}$ through the hardening law. Hence, in the frame of the Kocks–Mecking law, it writes

$$\sigma_y^{loc} = \begin{cases} \sigma_0 + \frac{\Theta_0}{\beta}\left[1 - \exp\left(-\beta\varepsilon_{acc}^{p\_loc}\right)\right] & \text{for } \sigma_y^{loc} \leqslant \sigma_y^{tr}, \\ \sigma_y^{tr} + \Theta_{IV}\left(\varepsilon_{acc}^{p\_loc} - \varepsilon_{acc}^{p\_tr}\right) & \text{for } \sigma_y^{loc} > \sigma_y^{tr}, \end{cases} \tag{31}$$

where

$$\varepsilon_{acc}^{p\_loc} \approx \int_0^t \sqrt{\frac{2}{3}\dot{\varepsilon}_{ij}^{loc}\dot{\varepsilon}_{ij}^{loc}}\mathrm{dt} \quad (i,j = r,\theta,z). \tag{32}$$

By using simple geometrical arguments, Fabrègue and Pardoen (2008, 2009) showed that the local strain rates next to the void surface, $\dot{\varepsilon}_{ij}^{loc}$, are linked to the applied strain rates, and to the evolution of the porosity f and the void aspect ratio W as

$$\dot{\varepsilon}_{\theta\theta}^{loc} = \frac{1}{3}\left(\dot{\varepsilon}_{zz} + 2\dot{\varepsilon}_{rr} + \frac{\dot{f}}{f} - \frac{\dot{W}}{W}\right), \tag{33}$$

$$\dot{\varepsilon}_{zz}^{loc} = \frac{\pi}{6}\left(\dot{\varepsilon}_{zz} + 2\dot{\varepsilon}_{rr} + \frac{\dot{f}}{f} + 2\frac{\dot{W}}{W}\right)\sqrt{\frac{1}{2}\left(\frac{1}{W^2}+1\right)}, \tag{34}$$

$$\dot{\varepsilon}_{rr}^{loc} = -\dot{\varepsilon}_{zz}^{loc} - \dot{\varepsilon}_{\theta\theta}^{loc}. \tag{35}$$

This version will be referred as the *version 2* of the Thomason model.

3.2.2. Assessment of the new extensions of the Thomason criterion

Fig. 12(a) shows the evolution of the left and right hand sides of the version 2 of the Thomason criterion given in Eq. (30), applied to unit cell calculations with $T = 1$, $W_0 = 1$, $\beta = 15$, $\Theta_0/\sigma_0 = 10$, for three different Θ_{IV} values. The onset of void coalescence corresponds to the point where the two sides of Eq. (30) intersect with each other. Note that the parameters used in Eqs. (29) and (30), i.e. χ, W and σ_{zz} are directly extracted from the cell calculations at each increment of the deformation. The local value σ_y^{loc} entering (30) is calculated using (32) to (35), while the value of σ_y entering (29) is calculated using (15). As explained earlier, the "exact" onset of coalescence is extracted directly from the change of the deformation mode in the unit cell calculations which corresponds to the point at which $\partial\varepsilon_{rr}/\partial\varepsilon_{zz}$ becomes suddenly very small (see Fig. 3), indicated by a filled circle in Fig. 12(a). For the present set of conditions, the coalescence strains predicted by the second form of the Thomason criterion are in very good agreement with the unit cell solution. Similar plots are obtained with the version 1.

In order to check the validity of the two versions of the Thomason criterion, the same comparison has been made for all the unit cell calculations performed in this work, involving different material properties and being loaded under different stress triaxialities, see Table A.1. In cases where the Thomason criterion does not predict the onset of coalescence before it is attained by the unit cell calculations, the quantities – extracted from the unit cell calculations – used in the criterion are linearly extrapolated as if coalescence did not start, until the Thomason criterion is satisfied. The comparison is made in Fig. 12(b) and the corresponding error is given in Fig. 12(c). As shown qualitatively in Fig. 12(b) and more quantitatively in Fig. 12(c), the Thomason criterion version 2 slightly overestimates the ductility at $T = 1$ by maximum 6%, while the version 1 has a tendency to underestimate it, by maximum 12%. At larger triaxiality, the quality of the predictions deteriorates. The version 1 of the criterion underestimates the results with a maximum error equal to 15% for $T = 2$ and 30% for $T = 3$, while the maximum error for version 2 is equal to 40% for $T = 2$ and 150% for $T = 3$. At large stress triaxiality, the extrapolation of the cell calculations results after the onset of coalescence becomes dubious and can explain part of the error associated with version 2. Nevertheless, it is clear that the predictions of version 2 are less satisfactory at large stress triaxiality. Note that the Thomason criterion version 1, Eq. (29), has a general tendency to underestimate the strain at the onset of coalescence, which is a good point to produce conservative predictions regarding integrity assessment analysis. On the contrary, the version 2, Eq. (30), generally overestimates the strain at coalescence, except in a few cases such as $T = 1$, $W_0 = 1/3$, $\Theta_0/\sigma_0 = 3$, $\beta = 15$ and $\Theta_{IV} = 0$, see Fig. 12(c).

4. Assessment of the full damage model and final discussion

The predictions of the integrated void growth and coalescence model are assessed by comparison to the finite element calculations. Fig. 13 (resp. Fig. 14(a,c,e)) presents results addressing different values of the stress triaxiality (resp. initial void aspect ratio). A filled circle • indicates the onset of coalescence predicted directly by the finite element calculations. The onset of coalescence predicted by applying the version 2 of the Thomason criterion (30) with all the parameters taken from the finite element calculations is indicated by a cross ×. The difference in strain between the filled circle and the cross indicates the error resulting only from the application of the void coalescence criterion. The onset of coalescence when combining the extended Gurson model and the version 1, Eq. (29) (resp. version 2, Eq. (30)) of the Thomason criterion is indicated by a square □ (resp. a circle ○) on the curve predicted by the constitutive model.

Fig. 13(a) and Fig. 14(a) give the variation of the axial stress σ_{zz} as a function of the axial strain ε_{zz}; the axial stress is well predicted during void growth, except for $T = 2$ and $T = 3$ for which the peak stress is slightly underestimated by the model. Regarding the onset of coalescence, the version 2 of the Thomason model (Eq. (30) is discussed first. Fig. 13(a) and Fig. 14(a) show that the coalescence model (30) provides accurate predictions at low stress triaxiality, whatever the initial void shape W_0, in agreement with Fig. 12(b). As a matter of fact, when the coalescence criterion is used together with the extended Gurson model, the error on the predicted onset of coalescence is mainly due to the error on the predicted porosity evolution

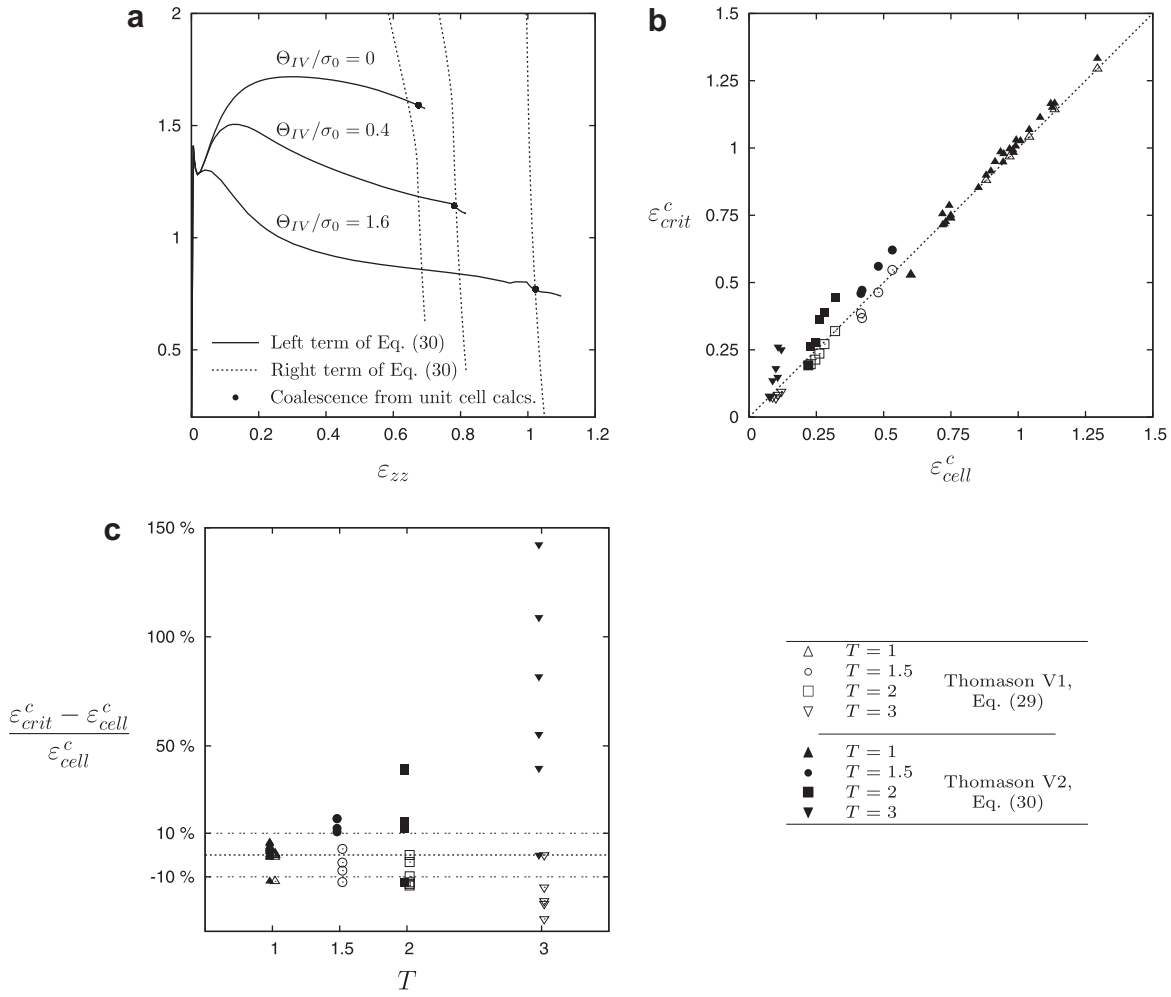

Fig. 12. (a) Evolution of the left and right sides of the Thomason criterion version 2 given in Eq. (30), applied to the unit cell calculations with $T = 1$, $W_0 = 1$, $\beta = 15$, $\Theta_0/\sigma_0 = 10$, for three different Θ_{IV} values. The filled circles • correspond to the strain at the onset of coalescence directly obtained by checking that $|\partial\varepsilon_{rr}/\partial\varepsilon_{zz}|$ becomes smaller than 5% of its value during the first part of the deformation. (b) Comparison of the strain value at the onset of coalescence ε^c_{crit}, predicted by both versions of the Thomason criterion, with ε^c_{cell} which corresponds to the condition $|\partial\varepsilon_{rr}/\partial\varepsilon_{zz}|$ very small, for unit cell calculations performed for a wide range of parameters given in Table A.1. (c) Variation of the error in ε^c_{crit} with respect to ε^c_{cell} as a function of stress triaxiality for the two versions of the void coalescence criterion.

and the other parameters entering the void growth model. More precisely, the origin of the discrepancy can be detected in Fig. 13(b) and Fig. 14(c): it essentially comes from inaccurate prediction of the porosity evolution after some amount of deformation. There is indeed an acceleration of the void growth rate due to void interaction effects which occurs before the onset of coalescence and which is not captured by the model. This observation agrees with earlier works of Koplik and Needleman (1988), and Pardoen and Hutchinson (2000).

Now, it is important to observe that the extra error coming from using the Gologanu model to predict the parameters entering version 1 of the coalescence criterion compared to the use of the parameters directly extracted from the cell calculations is significantly smaller than with version 2, see Fig. 13(a) and Fig. 14(a). The better behaviour of version 1 mostly appears when stage IV is accounted for. The fact that version 2 slightly overestimates the onset of coalescence when used with the exact evolution of the parameters (from the cell calculations) is amplified when adding the underestimation of the void growth rate at large strains coming from the Gologanu model. A simple remedy is to increase the value of α in Eq. (30) but this was not attempted here. Indeed, the beauty of version 2 is to avoid the use of any fitting parameter. A more in depth analysis of the impact of strain hardening on the localization process between two voids is needed to make further progress in this area. For the time being, the full model with version 1 of the coalescence criterion can be used safely within the entire parameters space, while the full model with version 2 should be avoided at high stress triaxiality and at high value of stage IV.

Fig. 13(c) (resp. Fig. 14(e)) gives the evolution of the void aspect ratio W with the axial strain ε_{zz} for several values of the stress triaxiality T (resp. initial void aspect ratio W_0). The model reproduces well the opening of the voids during straining (i.e. W increases) at low stress triaxiality and the closing (i.e. W decreases) at high stress triaxiality.

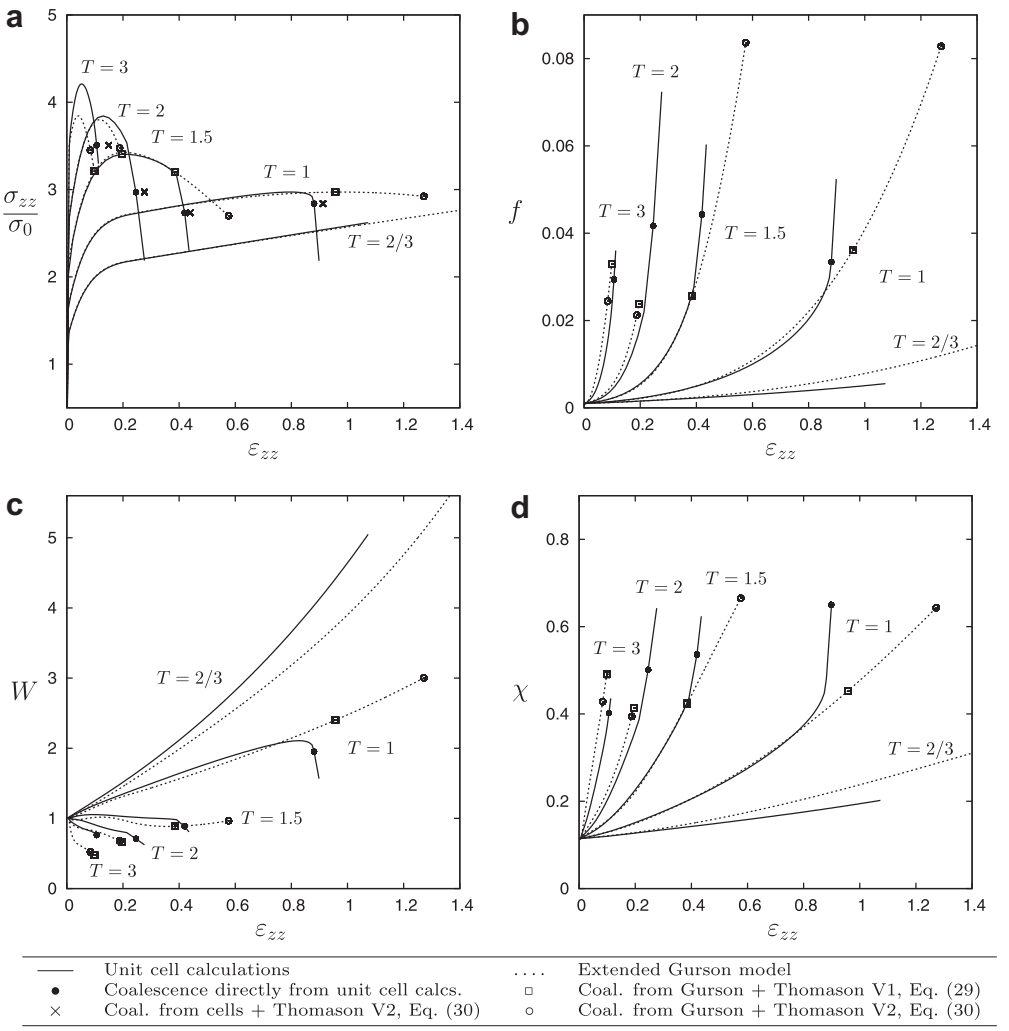

Fig. 13. Comparison between cell calculations and the full damage model regarding the stress triaxiality T. Variation with axial strain ε_{zz} of the (a) axial stress σ_{zz}, (b) porosity f, (c) void aspect ratio W, and (d) relative void spacing χ, with $W_0 = 1$, $\beta = 15$, $\Theta_0/\sigma_0 = 10$, $\Theta_{IV}/\sigma_0 = 0.4$.

Figs. 14(b,d,f) present results for different values of the stage IV hardening level Θ_{IV}. Fig. 14(f) shows that the void aspect ratio W evolution is better reproduced when $\Theta_{IV} > 0$. As a matter of fact, the h_T parameter used to fit the evolution of the void aspect ratio is less precisely fitted at low values of the incremental strain hardening exponent n_ε. When $\Theta_{IV} = 0$, n_ε has a low value during most of the straining history, see Fig. 10.

A direct comparison of these predictions to experimental results is not straightforward. Indeed, it is usually difficult to modify the strain hardening capacity of metals without affecting other characteristics which are playing a role in the ductile failure process. One example is given by precipitation hardening in Al alloys through which both the yield stress and strain hardening capacity are modified (Simar et al., 2007, 2010). Changing the initial yield stress can significantly alter the fracture behavior of a material, in addition to having a direct effect on the void growth rate and on the onset of coalescence due to differences in the strain hardening capacity. First, a lower yield stress gives rise to delayed void nucleation (e.g. Huber et al., 2005; Simar et al., 2010). Accurately predicting void nucleation is still a matter of open research and the comparison between the model and experiments will be affected also by the error coming from not capturing exactly this first step of the damage process, see also Tekoğlu and Pardoen (2010). Then, a high yield stress can favour the nucleation of a second population of voids which will accelerate the onset of void coalescence (e.g. Faleskog and Shih, 1997; Fabrègue and Pardoen, 2008, 2009; Gallais et al., 2007; Nielsen et al., 2010). The presence of a second population of voids can also modify the coalescence mode from internal necking to shear dominated, leading to a slant fracture (Asserin-Lebert et al., 2005; Faleskog and Shih, 1997). Hence, a direct analysis of the strain hardening effect on ductile failure requires an ideal material where void nucleation takes place at small stress levels (or with voids already present in the microstructure) and without any secondary population of particles. One example has been given in the case of extruded copper rods, involving a fraction of percent of micron sized copper oxide inclusions, with a poor interface resistance with the matrix (Pardoen and Delannay, 1998; Pardoen et al., 1998).

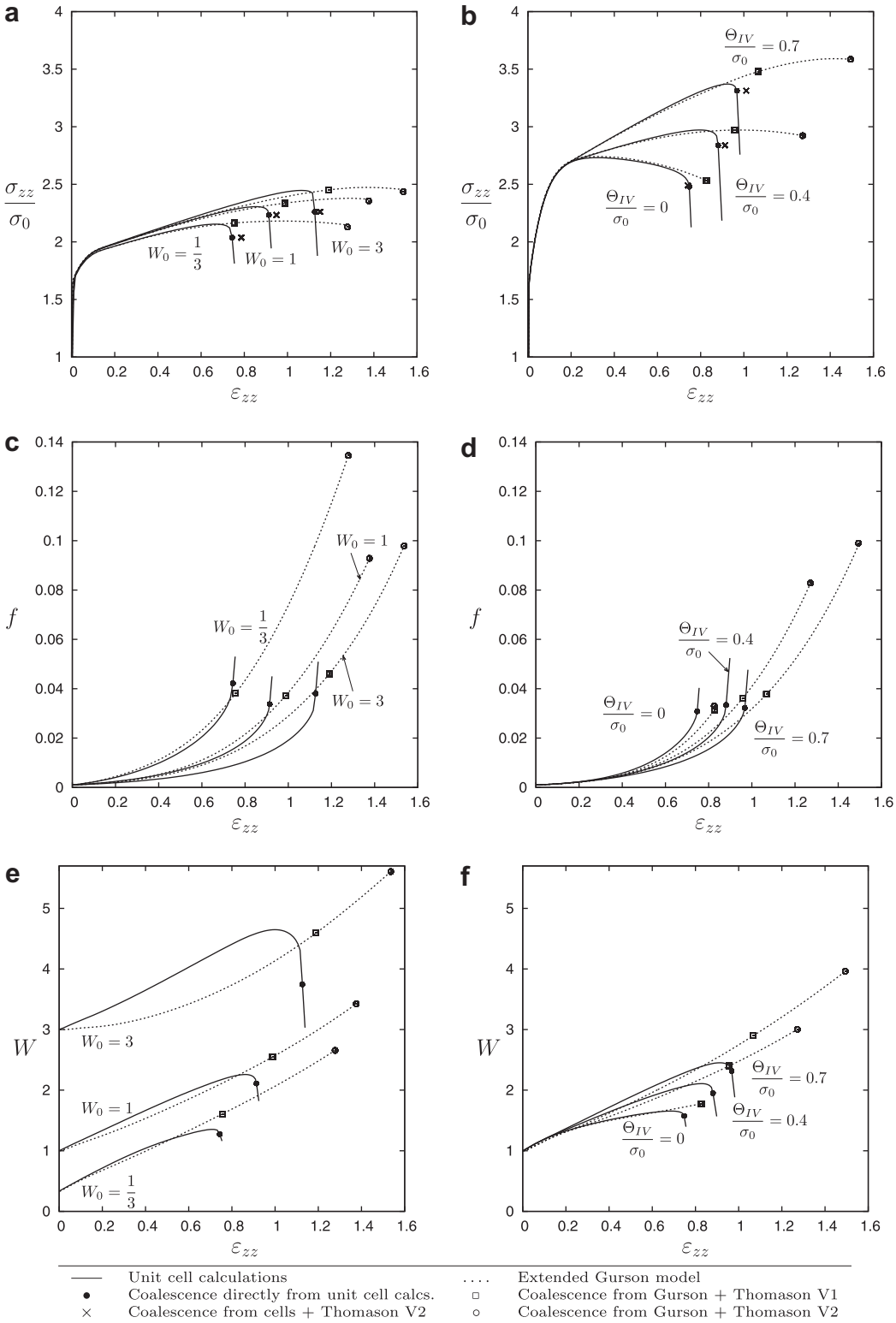

Fig. 14. Comparison between cell calculations and the full damage model regarding (a,c,e) the initial void aspect ratio W_0, and (b,d,f) the stage IV hardening rate Θ_{IV}. Variation with axial strain of the (a,b) axial stress, (c,d) porosity, and (e,f) void aspect ratio, with $T = 1$, $\beta = 15$, (a,c,e) $\Theta_0/\sigma_0 = 3$, $\Theta_{IV}/\sigma_0 = 0.4$, and (b,d,f) $W_0 = 1$, $\Theta_0/\sigma_0 = 10$.

As-received samples had a high strength but low strain hardening capacity while annealed samples involved a high strain hardening capacity and low strength (the strain-hardening evolution was modelled using a two parts power law hardening fit). At the same stress triaxiality, the annealed samples presented a ductility higher by at least 20% compared to the as-received samples.

A final point of discussion concerns the validity of using a Kocks–Mecking formalism to describe the strain hardening around growing voids. If the voids are too small compared to the grain size, single crystal plasticity effects will play an important role and grain orientation with respect to the loading configuration can significantly affect the evolution of f and W (Yerra et al., 2010). If the voids are small compared to the intrinsic length of the dislocation structure, the averaging response underlying the Kocks–Mecking model will not be fully valid anymore and more sophisticated analysis will be needed. Recently, both the strain gradient plasticity theory (Borg et al., 2008) and the dislocation dynamics method (Segurado and LLorca, 2010) have been used to simulate void growth. Now, when the Kocks–Mecking formalism can be safely used, one of the interest is then to use extended versions of the Kocks–Mecking model in order to account for instance for precipitates hardening (Simar et al., 2007) or grain size effects (Delincé et al., 2007), or to couple the model with lower scale simulations, e.g. Naamane et al. (2010), to provide a link with the dislocation dynamics and intrinsic mechanisms of plasticity with respect to real microstructures.

5. Conclusions

The effect of strain hardening –as described via a physics based stage III and stage IV Kocks–Mecking model– on void growth and coalescence has been addressed using FE cell calculations. The main finding is that the effect of stage IV hardening, which will usually be attained either globally at low stress triaxiality, or at least locally around the voids at large stress triaxiality, can be very significant. When comparing the cases of no stage IV and early onset of stage IV, the void growth rate can change by a factor of two, hence the ductility. This shows that the use of a simple hardening law with improper extrapolation to large strains can introduce major errors in the predicted fracture strains. Furthermore, properly accounting for stage IV can have a significant effect on the prediction of the void nucleation kinetics if void nucleation takes place at large strains.

The ductile failure model, based on the GLD model for void growth and on two versions of the Thomason criterion for coalescence, has been coupled to a Kocks–Mecking type hardening law involving stage III and stage IV. The final model gives reasonable predictions over a wide range of parameters.

This study opens the road to the development of more realistic continuum damage models based on physics, and microstructure informed hardening laws. This is important in the context of building chain models which start from the microstructure evolution during processing and end with the predictions of the end use properties involving the fracture strain.

Acknowledgements

Fruitful discussions about the present study with A. Simar regarding Kocks–Mecking strain hardening and with L. Delannay regarding the method used to impose a constant stress triaxiality are gratefully acknowledged. We thank one anonymous reviewer for his suggestion regarding the fitting function f_{sh}. L. Lecarme acknowledges the financial support of the Belgian Interuniversity Attraction Pole (IAP) P6/24 and of the Walloon Region through the Winnomat 2 Fabulous project. C. Tekoğlu acknowledges the financial support from the Belgian Fond National de la Recherche Scientifique (FNRS) through a post-doc grant related to the Hetmat network project. Calculations have been performed on the CISM-UCL Belgium computer facilities through project FRFC 2-4556-99 with FNRS.

Appendix A. Alternative expression of f_{sh}

The parameter q_b is mostly sensitive to the void shape, see e.g. Søvik and Thaulow (1997), and as shown in Fig. 7 has almost no effect on the evolution of either the void aspect ratio W or the porosity f; therefore, f_{sh} is assumed to be independent of the athermal hardening parameter Θ_0. An expression for the heuristic parameter f_{sh} is obtained by comparing the predictions of the GLD model with the results of unit cell calculations in terms of the best agreement in the void growth rate, mainly in the early stage of straining. In the cell calculations, while changing the values of β and Θ_{IV} for each calculation, other parameters are kept constant at intermediate values, $T = 1$, $W_0 = 1$, $\Theta_0/\sigma_0 = 10$. Based on this comparison, the following expression is suggested for f_{sh}:

$$(f_{sh})^{\mathrm{III}} = \begin{cases} 0.1 + (\ln\beta - 0.91)\left(-0.18\,\frac{\Theta_{IV}}{\sigma_0} + 0.3\right) & \text{for } \beta > 2.5, \\ 0.1 & \text{for } \beta \leqslant 2.5, \end{cases} \tag{A-1}$$

$$(f_{sh})^{\mathrm{IV}} = 0.35 \quad \text{for } \Theta_{IV} > 0. \tag{A-2}$$

Note that f_{sh} is equal to $(f_{sh})^{\mathrm{III}}$ during stage III, and to $(f_{sh})^{\mathrm{IV}}$ after entering stage IV. Also, Eqs. (A-1) and (A-2) are valid in the range $0 \leqslant \Theta_{IV}/\sigma_0 \leqslant 1$. Figs. A1(a) and (b) show, respectively, the accuracy of Eqs. (A-1) and (A-2) in comparison with the FE unit cell calculations for the evolution of $(f_{sh})^{\mathrm{III}}$ and $(f_{sh})^{\mathrm{IV}}$, as a function of β, for different Θ_{IV} values.

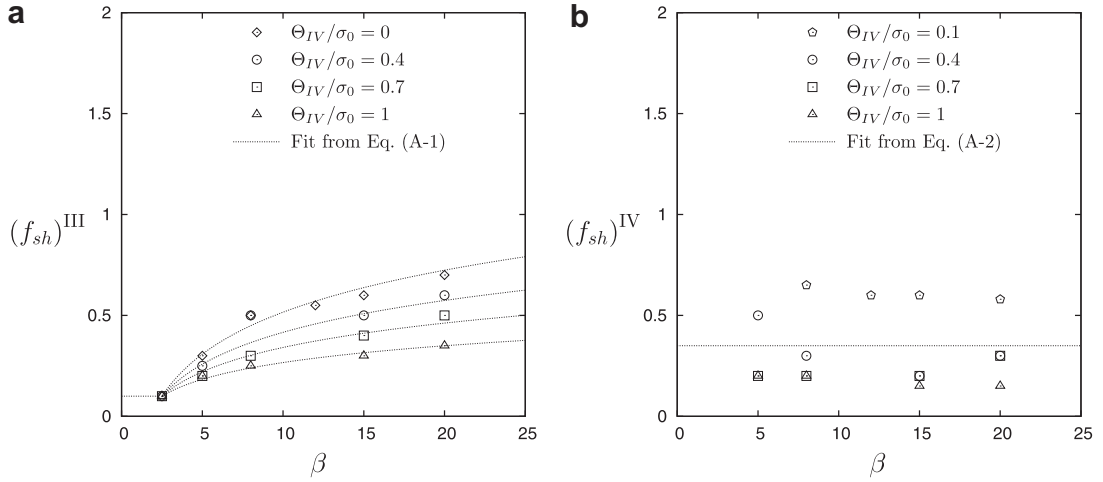

Fig. A1. Comparison of (a) Eq. (A-1) and (b) Eq. (A-2) with the results of the FE unit cell calculations for the evolution of, respectively, $(f_{sh})^{III}$ and $(f_{sh})^{IV}$, as a function of the dynamic recovery rate β, for different Θ_{IV} values. For all the calculations $T = 1$, $W_0 = 1$, and $\Theta_0/\sigma_0 = 10$. Each data point represents the (f_{sh}) value providing the best agreement between the GLD model and one unit cell calculation.

References

ABAQUS, 2008. Abaqus Theory Manual, Version 6.8. Providence, Rhode Island: Dassault Systèmes.

Argon, A., 2008. Strengthening Mechanisms in Crystal Plasticity. Oxford University Press, New York.

Asserin-Lebert, A., Besson, J., Gourgues, A., 2005. Fracture of 6056 aluminum sheet materials: effect of specimen thickness and hardening behavior on strain localization and toughness. Mater. Sci. Eng. A 395 (1–2), 186–194.

Badreddine, H., Saanouni, K., Dogui, A., 2010. On non-associative anisotropic finite plasticity fully coupled with isotropic ductile damage for metal forming. Int. J. Plast. 26 (11), 1541–1575.

Benzerga, A.A., 2000. Rupture ductile des tôles anisotropes, simulation de la propagation longitudinale dans une tôle pressurisée. Ph.D. thesis, Ecole des Mines de Paris.

Benzerga, A.A., Besson, J., 2001. Plastic potentials for anisotropic porous solids. Eur. J. Mech. A. Solids 20 (3), 397–434.

Benzerga, A.A., Leblond, J.-B., 2010. Ductile fracture by void growth to coalescence. Adv. Appl. Mech. 44, 169–305.

Benzerga, A.A., Besson, J., Pineau, A., 2004. Anisotropic ductile fracture. Part II: theory. Acta Mater. 52 (15), 4639–4650.

Besson, J., 2009. Damage of ductile materials deforming under multiple plastic or viscoplastic mechanisms. Int. J. Plast. 25 (11), 2204–2221.

Besson, J., Guillemer-Neel, C., 2003. An extension of the Green and Gurson models to kinematic hardening. Mech. Mater. 35 (1–2), 1–18.

Borg, U., Niordson, C.F., Kysar, J.W., 2008. Size effects on void growth in single crystals with distributed voids. Int. J. Plast. 24 (4), 688–701.

Brocks, W., Sun, D.Z., Hönig, A., 1995. Verification of the transferability of micromechanical parameters by cell model calculations with visco-plastic materials. Int. J. Plast. 11 (8), 971–989.

Byun, T., Hashimoto, N., Farrell, K., 2004. Temperature dependence of strain hardening and plastic instability behaviors in austenitic stainless steels. Acta Mater. 52 (13), 3889–3899.

Chéhab, B., Bréchet, Y., Véron, M., Jacques, P., Parry, G., Mithieux, J.-D., Glez, J.-C., Pardoen, T., 2010. Micromechanics of high-temperature damage in dual-phase stainless steel. Acta Mater. 58 (2), 626–637.

Chu, C.C., Needleman, A., 1980. Void nucleation effects in biaxially stretched sheets.. J. Eng. Mater. Technol. 102 (3), 249–256.

Delincé, M., Bréchet, Y., Embury, J., Geers, M., Jacques, P., Pardoen, T., 2007. Structure-property optimization of ultrafine-grained dual-phase steels using a microstructure-based strain hardening model. Acta Mater. 55 (7), 2337–2350.

Fabrègue, D., Pardoen, T., 2008. A constitutive model for elastoplastic solids containing primary and secondary voids. J. Mech. Phys. Solids 56 (3), 719–741.

Fabrègue, D., Pardoen, T., 2009. Corrigendum to "A constitutive model for elastoplastic solids containing primary and secondary voids [J. Mech. Phys. Solids 56 (2008) 719–741]. J. Mech. Phys. Solids 57 (5), 869–870.

Faleskog, J., Shih, C.F., 1997. Micromechanics of coalescence. I: synergistic effects of elasticity, plastic yielding and multi-size-scale voids. J. Mech. Phys. Solids 45 (1), 21–25.

Gallais, C., Simar, A., Fabrègue, D., Denquin, A., Lapasset, G., de Meester, B., Bréchet, Y., Pardoen, T., 2007. Multiscale analysis of the strength and ductility of AA 6056 aluminum friction stir welds. Metall. Mater. Trans. A 38A (5), 964–981.

Gao, X., Faleskog, J., Shih, C.F., Dodds, R.H., 1998. Ductile tearing in part-through cracks: experiments and cell-model predictions. Eng. Fract. Mech. 59 (6), 761–777.

Gil Sevillano, J., van Houtte, P., Aernoudt, E., 1980. Large strain work hardening and textures. Prog. Mater Sci. 25 (2–4), 69–412.

Gologanu, M., Leblond, J.-B., Devaux, J., 1993. Approximate models for ductile metals containing non-spherical voids – case of axisymmetric prolate ellipsoidal cavities. J. Mech. Phys. Solids 41, 1723–1754.

Gologanu, M., Leblond, J.-B., Devaux, J., 1994. Approximate models for ductile metals containing non-spherical voids – case of axisymmetric oblate ellipsoidal cavities. J. Eng. Mat. Tech. 116, 290–297.

Gologanu, M., Leblond, J.-B., Perrin, G., Devaux, J., 1997. Recent extensions of Gurson's model for porous ductile metals. In: Suquet, P. (Ed.), Continuum Micromechanics. Springer-Verlag, New York, pp. 61–130.

Gurson, A.L., 1977a. Continuum theory of ductile rupture by void nucleation and growth. I: Yield criteria and flow rules for porous ductile media. J. Eng. Mater. Technol. 99 (1), 2–15.

Gurson, A.L., 1977b. Porous rigid-plastic materials containing rigid inclusions – Yield function, plastic potential, and void nucleation. In: Taplin, D.M.R. (Ed.), Proceedings of International Conferefnce on Fracture, vol. 2A. Pergamon Press, Oxford, p. 357.

Huber, G., Bréchet, Y., Pardoen, T., 2005. Predictive model for void nucleation and void growth controlled ductility in quasi-eutectic cast aluminium alloys. Acta Mater. 53 (9), 2739–2749.

Keralavarma, S.M., Benzerga, A.A., 2008. An approximate yield criterion for anisotropic porous media. C.R. Mec. 336 (9), 685–692.

Keralavarma, S., Benzerga, A., 2010. A constitutive model for plastically anisotropic solids with non-spherical voids. J. Mech. Phys. Solids 58 (6), 874–901.

Klöcker, H., Tvergaard, V., 2003. Growth and coalescence of non-spherical voids in metals deformed at elevated temperature. Int. J. Mech. Sci. 45 (8), 1283–1308.
Kocks, U.F., Mecking, H., 2003. Physics and phenomenology of strain hardening: the FCC case. Prog. Mater Sci. 48 (3), 171–273.
Koplik, J., Needleman, A., 1988. Void growth and coalescence in porous plastic solids. Int. J. Solids Struct. 24 (8), 835–853.
Lassance, D., Scheyvaerts, F., Pardoen, T., 2006. Growth and coalescence of penny-shaped voids in metallic alloys. Eng. Fract. Mech. 73 (8), 1009–1034.
Lassance, D., Fabrègue, D., Delannay, F., Pardoen, T., 2007. Micromechanics of room and high temperature fracture in 6xxx Al alloys. Prog. Mater Sci. 52 (1), 62–129.
Leblond, J.-B., Mottet, G., 2008. A theoretical approach of strain localization within thin planar bands in porous ductile materials. C.R. Mec. 336 (1–2), 176–189.
Leblond, J.-B., Perrin, G., Devaux, J., 1995. An improved Gurson-type model for hardenable ductile metals. Eur. J. Mech. A. Solids 14 (4), 499–527.
Lin, R.C., Steglich, D., Brocks, W., Betten, J., 2006. Performing RVE calculations under constant stress triaxiality for monotonous and cyclic loading. Int. J. Numer. Methods Eng. 66 (8), 1331–1360.
McClintock, F.A., 1968. A criterion for ductile fracture by the growth of holes. J. Appl. Mech. 35, 363–371.
Mear, M., Hutchinson, J., 1985. Influence of yield surface curvature on flow localization in dilatant plasticity. Mech. Mater. 4 (3–4), 395–407.
Mecking, H., Kocks, U., 1981. Kinetics of flow and strain-hardening. Acta Metall. 29 (11), 1865–1875.
Monchiet, V., Gruescu, C., Charkaluk, E., Kondo, D., 2006. Approximate yield criteria for anisotropic metals with prolate or oblate voids. C.R. Mec. 334 (7), 431–439.
Monchiet, V., Cazacu, O., Charkaluk, E., Kondo, D., 2008. Macroscopic yield criteria for plastic anisotropic materials containing spheroidal voids. Int. J. Plast. 24 (7), 1158–1189.
Naamane, S., Monnet, G., Devincre, B., 2010. Low temperature deformation in iron studied with dislocation dynamics simulations. Int. J. Plast. 26 (1), 84–92.
Nahshon, K., Hutchinson, J., 2008. Modification of the Gurson model for shear failure. Eur. J. Mech. A. Solids 27 (1), 1–17.
Nielsen, K., Pardoen, T., Tvergaard, V., de Meester, B., Simar, A., 2010. Modelling of plastic flow localization and damage development in friction stir welded 6005A aluminium alloy using physics based strain hardening law. Int. J. Solids Struct. 47 (18–19), 2359–2370.
Pardoen, T., 2006. Numerical simulation of low stress triaxiality ductile fracture. Comput. Struct. 84 (26–27), 1641–1650.
Pardoen, T., Brechet, Y., 2004. Influence of microstructure-driven strain localization on the ductile fracture of metallic alloys. Philos. Mag. 84 (3), 269–297.
Pardoen, T., Delannay, F., 1998. Assessment of void growth models from porosity measurements in cold-drawn copper bars. Metall. Mater. Trans. A 29 (7), 1895–1909.
Pardoen, T., Hutchinson, J.W., 2000. An extended model for void growth and coalescence. J. Mech. Phys. Solids 48 (12), 2467–2512.
Pardoen, T., Hutchinson, J.W., 2003. Micromechanics-based model for trends in toughness of ductile metals. Acta Mater. 51 (1), 133–148.
Pardoen, T., Doghri, I., Delannay, F., 1998. Experimental and numerical comparison of void growth models and void coalescence criteria for the prediction of ductile fracture in copper bars. Acta Mater. 46 (2), 541–552.
Pardoen, T., Marchal, Y., Delannay, F., 1999. Thickness dependence of cracking resistance in thin aluminium plates. J. Mech. Phys. Solids 47 (10), 2093–2123.
Pardoen, T., Hachez, F., Marchioni, B., Blyth, P.H., Atkins, A.G., 2004. Mode I fracture of sheet metal. J. Mech. Phys. Solids 52 (2), 423–452.
Rauch, E.F., 2009. Plastic behavior of metals at large strains: Experimental studies involving simple shear. J. Eng. Mater. Technol. 131 (1), 011107–011108.
Rice, J.R., Tracey, D.M., 1969. On the ductile enlargement of voids in triaxial stress fields. J. Mech. Phys. Solids 17 (3), 201–217.
Scheyvaerts, F., Pardoen, T., Onck, P.R., 2010b. A new model for void coalescence by internal necking. Int. J. Damage Mech. 19 (1), 95–126.
Scheyvaerts, F., Onck, P., Tekoğlu, C., Pardoen, T., 2011. The growth and coalescence of voids under combined shear and tension. J. Mech. Phys. Solids 59 (2), 373–397.
Segurado, J., LLorca, J., 2010. Discrete dislocation dynamics analysis of the effect of lattice orientation on void growth in single crystals. Int. J. Plast. 26 (6), 806–819.
Simar, A., Bréchet, Y., de Meester, B., Denquin, A., Pardoen, T., 2007. Sequential modeling of local precipitation, strength and strain hardening in friction stir welds of an aluminum alloy 6005A-T6. Acta Mater. 55 (18), 6133–6143.
Simar, A., Nielsen, K., de Meester, B., Tvergaard, V., Pardoen, T., 2010. Micro-mechanical modelling of ductile failure in 6005A aluminium using a physics based strain hardening law including stage IV. Eng. Fract. Mech. 77 (13), 2491–2503.
Søvik, O.P., Thaulow, C., 1997. Growth of spheroidal voids in elastic-plastic solids. Fatigue Fract. Eng. Mater. Struct. 20 (12), 1731–1744.
Steglich, D., Brocks, W., Heerens, J., Pardoen, T., 2008. Anisotropic ductile fracture of Al 2024 alloys. Eng. Fract. Mech. 75 (12), 3692–3706.
Tekoğlu, C., Pardoen, T., 2010. A micromechanics based damage model for composite materials. Int. J. Plast. 26 (4), 549–569.
Thomason, P., 1985. A three-dimensional model for ductile fracture by the growth and coalescence of microvoids. Acta Metall. 33 (6), 1087–1095.
Thomason, P., 1990. Ductile Fracture of Metals. Pergamon press.
Tvergaard, V., 1981. Influence of voids on shear band instabilities under plane strain conditions. Int. J. Fract. 17 (4), 389–407.
Tvergaard, V., 1982. On localization in ductile materials containing spherical voids. Int. J. Fract. 18 (4), 237–252.
Tvergaard, V., Hutchinson, J.W., 2002. Two mechanisms of ductile fracture: void by void growth versus multiple void interaction. Int. J. Solids Struct. 39 (13–14), 3581–3597.
Tvergaard, V., Needleman, A., 1984. Analysis of the cup-cone fracture in a round tensile bar. Acta Metall. 32 (1), 157–169.
Voce, E., 1955. A practical strain-hardening function. Metallurgia 51, 219–226.
Wen, J., Huang, Y., Hwang, K.C., Liu, C., Li, M., 2005. The modified Gurson model accounting for the void size effect. Int. J. Plast. 21 (2), 381–395.
Worswick, M.J., Pick, R.J., 1990. Void growth and constitutive softening in a periodically voided solid. J. Mech. Phys. Solids 38 (5), 601–625.
Yerra, S., Tekoğlu, C., Scheyvaerts, F., Delannay, L., Van Houtte, P., Pardoen, T., 2010. Void growth and coalescence in single crystals. Int. J. Solids Struct. 47 (7–8), 1016–1029.
Zehetbauer, M., Seumer, V., 1993. Cold work hardening in stages IV and V of F. C.C. metals. I: Experiments and interpretation. Acta Metall. Mater. 41 (2), 577–588.
Zhang, Z.L., Niemi, E., 1995. A new failure criterion for the Gurson–Tvergaard dilational constitutive model. Int. J. Fract. 70 (4), 321–334.